SINGULAR OPTICS OF FOCUSED FIELDS

BY

ROBERT W. SCHOONOVER

B.S., University of Illinois at Urbana-Champaign, 2004

THESIS

Submitted in partial fulfillment of the requirements
for the degree of Master of Science in Electrical and Computer Engineering
in the Graduate College of the
University of Illinois at Urbana-Champaign, 2006

Urbana, Illinois

SINGULAR OPTICS OF FOCUSED FIELDS

Approved by
Prof. P. Scott Carney

_____

_____

To Katrina, who was more understanding about my year abroad than she had any right to be

ACKNOWLEDGMENTS

I am first grateful to the U.S. Fulbright Program for funding my year abroad, studying at Vrije Universiteit in Amsterdam. Drs. Linda Pietersen was especially helpful in making the transition painless.

John Barnes Linnet was an invaluable resource in assembling the appendices for this thesis.

Thank you to my parents, Jack and Sue Schoonover, who have supported me in all my academic pursuits. They have encouraged my curiosity and thirst for knowledge, even when it takes me far away, and I will be eternally grateful for that.

Thank you to Prof. Taco Visser of Vrije Universiteit who advised me in much of this work. Beyond being a good advisor, he and his wife Anja made my stay in the Netherlands infinitely more hospitable and enjoyable. I am also grateful to Prof. Visser for the use of figures he created that are scattered throughout this thesis.

Last, thanks must go to Prof. P. Scott Carney, my advisor. He has encouraged my academic pursuits and been a good friend, as well as advisor, for the past three years. He encouraged my year abroad and helped make it a success.

TABLE OF CONTENTS

CHAPTER 1

INTRODUCTION

At points in complex-valued scalar fields where the amplitude is zero, the phase of the field is undetermined or singular [1]. Singular optics is concerned with the description and classification of the different kinds of singularities that can occur in wave fields [2, 3]. Examples of such singularities are the zeros of intensity that are found in focused fields [4]. In real-valued, two-dimensional vector fields, the orientation of the vector is singular wherever the vector vanishes. Such singularities of the Poynting vector field in two-dimensional geometries are studied in Refs. [5, 6, 7]. Complex-valued vector fields can display singularities of the vector components. Examples of these are singularities of the longitudinal component of the electric field in strongly focused, linearly polarized beams [8]. Recently, the two-point correlation functions that describe spatially partially coherent light were shown to posses singularities as well [9, 10, 11, 12]. All types of singularities mentioned above can be created or annihilated when a system parameter, such as the wavelength of the field, is smoothly varied.

Because of their use in, for example, optical trapping, the properties of focused, radially polarized beams have been studied extensively in the past few years (see, e.g., [13] and the references therein).

This thesis is an expansion of two previously published papers [14, 15]. As will be shown in Ch. 2, the electric field in the focal region of a radially polarized beam has two non-zero parts, namely, a radial component and a longitudinal component. The magnetic field remains azimuthal upon focusing. To analyze radially polarized beams in more detail, this thesis considers the case of the superposition of two orthogonal, Hermite-Gauss beams. The

system parameters, the semiaperture angle and the beam width, will be varied to create and annihilate various singularities. The two components of the electric field and the one component of the magnetic field will be analyzed through the methods of singular optics. The electric field, however, cannot be treated as a scalar. At every point in a time-harmonic electromagnetic field, the end point of the electric field vector traces out an ellipse as time progresses [16, Sec. 1.4]. The polarization is said to be singular at points where this ellipse degenerates into a circle (at so-called C-points) or into a line (at so-called L-lines). Polarization singularities in wave fields are described in Refs. [2], and [17, 18, 19, 20, 21]. These polarization singularities will be analyzed in Ch. 4. In Ch. 5, singularities of the Poynting vector for such radially polarized fields will be examined and related to the phase singularities and polarization singularities previously studied.

CHAPTER 2

FOCUSING AND SINGULAR OPTICS

The structure of the total electomagnetic field is, generally, a very complicated topic. There are three components for the electric and magnetic fields, and they are related through Maxwell's equations [16]. In the case of paraxial electromagnetics, in which the z-component of both the electric and magnetic fields is assumed to be zero (or at least insignificant), there are four nonzero components that must be dealt with. The focusing of such fields has been thoroughly studied under the DeBye approximation for many years [13, 16, 22]. The process of focusing a paraxial field introduces nontrivial electric and magnetic fields in the z-direction in the focal region, and the longitudinal fields have been of much interest recently [13, 23, 24, 25, 26]. In the case of a radially polarized beam, it has been found that the electric field has two nonzero components - a radial component and a longitudinal component. The associated magnetic field is nonzero only for the azimuthal component (all in cylindrical coordinates). With only three nontrivial field components, radially polarized fields (and, likewise, azimuthally polarized fields, which are not discussed in this thesis) are ideal for study because of their relative simplicity.

2.1 Focusing

Consider an aplanatic focusing system L, as depicted in Fig. 2.1. The system has a focal length f and a semiaperture angle α. The origin O of a right-handed Cartesian coordinate system is taken to be at the geometrical focus. A monochromatic, radially polarized beam is incident on the system. The electric and magnetic fields at time t at position $\mathbf{r}$ are given

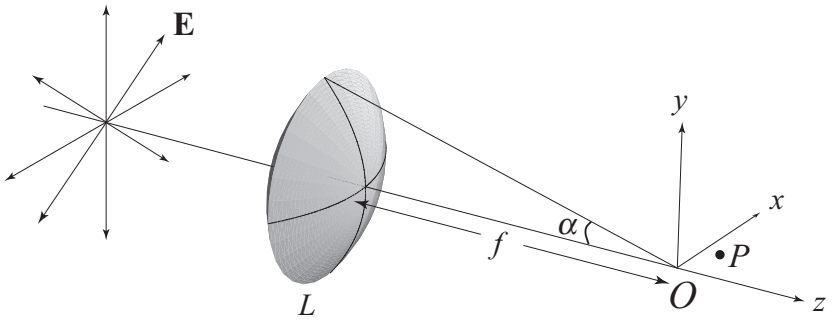

Figure 2.1: Illustration of a high numerical aperture system focusing a radially polarized beam.

by the expressions

$$\mathbf{E}(\mathbf{r},t) = \mathrm{Re}\left[\mathbf{e}(\mathbf{r})\exp(-\mathrm{i}\omega t)\right], \tag{2.1}$$

$$\mathbf{H}(\mathbf{r},t) = \mathrm{Re}\left[\mathbf{h}(\mathbf{r})\exp(-\mathrm{i}\omega t)\right], \tag{2.2}$$

respectively, where Re denotes the real part. The longitudinal component e_z and the radial component e_ρ of the electric field at a point $P = (\rho_P, z_P)$ in the focal region are given by the equations [13]

$$\begin{aligned} e_z(\rho_P, z_P) &= -\mathrm{i}kf\int_0^\alpha l(\theta)\sin^2\theta\cos^{1/2}\theta \\ &\quad \times \exp(\mathrm{i}kz_P\cos\theta)J_0\left(k\rho_P\sin\theta\right)\,\mathrm{d}\theta, \end{aligned} \tag{2.3}$$

$$\begin{aligned} e_\rho(\rho_P, z_P) &= -kf\int_0^\alpha l(\theta)\sin\theta\cos^{3/2}\theta \\ &\quad \times \exp(\mathrm{i}kz_P\cos\theta)J_1\left(k\rho_P\sin\theta\right)\,\mathrm{d}\theta, \end{aligned} \tag{2.4}$$

where J_i is the Bessel function of the first kind of order i. Also, $l(\theta)$ denotes the angular amplitude function

$$l(\theta) = f\sin\theta\exp(-f^2\sin^2\theta/w_0^2), \tag{2.5}$$

where w_0 is the spot size of the beam in the waist plane, which is assumed to coincide with the entrance plane of the focusing system. As stated above, the electric field has no azimuthal component. On using the dimensionless optical coordinates (sometimes referred

to as *Lommel variables*)

$$u = kz_P \sin^2\alpha, \tag{2.6}$$

$$v = k\rho_P \sin\alpha, \tag{2.7}$$

to specify the position of the observation point P, Eqs. (2.3) and (2.4) can be rewritten as

$$\begin{aligned} e_z(u,v) &= -\mathrm{i}kf^2 \int_0^\alpha \sin^3\theta \cos^{1/2}\theta \exp(-\beta^2 \sin^2\theta) \\ &\quad \times \exp(\mathrm{i}u\cos\theta/\sin^2\alpha) J_0\left(\frac{v\sin\theta}{\sin\alpha}\right) \mathrm{d}\theta, \end{aligned} \tag{2.8}$$

$$\begin{aligned} e_\rho(u,v) &= -kf^2 \int_0^\alpha \sin^2\theta \cos^{3/2}\theta \exp(-\beta^2 \sin^2\theta) \\ &\quad \times \exp(\mathrm{i}u\cos\theta/\sin^2\alpha) J_1\left(\frac{v\sin\theta}{\sin\alpha}\right) \mathrm{d}\theta, \end{aligned} \tag{2.9}$$

where the parameter $\beta = f/w_0$ denotes the ratio of the focal length of the system and the spot size of the beam in the waist plane.

The magnetic field can then be found through Maxwell's Equations in free space [16, Sec. 3.1.1 Eqs. (2-3)]

$$\nabla \times \mathbf{H} + \mathrm{i}k\epsilon\mathbf{E} = 0 \tag{2.10}$$

$$\nabla \times \mathbf{E} - \mathrm{i}k\mu\mathbf{H} = 0 \tag{2.11}$$

and Eqs. (2.3-2.4):

$$\begin{aligned} h_\phi(\rho_P, z_P) &= \frac{-\mathrm{i}}{k\mu}\left(\frac{\partial e_\rho}{\partial z_P} - \frac{\partial e_z}{\partial \rho_P}\right) \\ &= \frac{-kf}{\mu}\int_0^\alpha l(\theta)\sin(\theta)\cos^{1/2}\theta \\ &\quad \times \exp(\mathrm{i}kz_P\cos\theta) J_1\left(k\rho_P\sin\theta\right) \mathrm{d}\theta. \end{aligned} \tag{2.12}$$

The form of the magnetic field in optical coordinates is thus

$$\begin{aligned} h_\phi(u,v) &= \frac{-kf^2}{\mu}\int_0^\alpha \sin^2(\theta)\cos^{1/2}\theta \exp(-\beta^2\sin^2\theta) \\ &\quad \times \exp(\mathrm{i}u\cos\theta/\sin^2\alpha) J_1\left(\frac{v\sin\theta}{\sin\alpha}\right) \mathrm{d}\theta. \end{aligned} \tag{2.13}$$

Equations (2.8-2.9) and (2.13), with coordinates (u, v) and system parameters α and β are fields that will be analyzed in the rest of this thesis.

2.2 Singular Optics for Scalar Fields

Singular optics [2, 3] deals with the way in which fields behave around singular points - points where quantities such as phase angles of a wave field or the orientation angle of the polarization ellipse are indeterminate. Each component of the electromagnetic field can be described as a complex scalar quantity with both magnitude and phase. In the rest of this chapter, each of the three nonzero components will be briefly discussed in terms of its singular points.

Any complex number can be represented in a variety of forms. One particularly useful representation is to express it as an amplitude and associated phase

$$A(\mathbf{r}) = |A(\mathbf{r})| \exp[\mathrm{i}\phi(\mathbf{r})], \tag{2.14}$$

where $|A|$ is the magnitude of the complex number A and ϕ is the phase. When $|A|$ is identically zero, the real scalar ϕ has no meaning - it is singular! However, in the vicinity of such a singular point, the phase behaves in one of a few well-established ways [2]. These singularities have a so-called topological charge s defined by

$$s = \frac{1}{2\pi} \oint_C \nabla\phi(\mathbf{r}) \cdot \mathrm{d}\mathbf{r} \tag{2.15}$$

and a topological index t defined as the topological charge of the vector field $\nabla\phi(\mathbf{r})$. The direction in which the contour integral is taken is somewhat arbitrary, although it should be consistent throughout any analysis. The direction will only affect the values of s, not t. Phase singularities have charge $s = \pm 1$ and index $t = 1$. Phase saddles - points where the phase is defined but its gradient is not - have $s = 0$ and $t = -1$.

Singular points can be created and annihilated through the process of changing a system parameter. In the case of this thesis, that usually involves changing the semiaperture angle α. Singularities cannot be annihilated or created singly, however. There must be a conservation of both charge and index. Therefore, the simplest annihilation involves two phase singularities and two phase saddles such that $s_{total} = 0$ and $t_{total} = 0$ when summed among all four singularities. Of course, more involved annihilations are possible, but these can always be recast as multiple separate annihilations occurring at the same point.

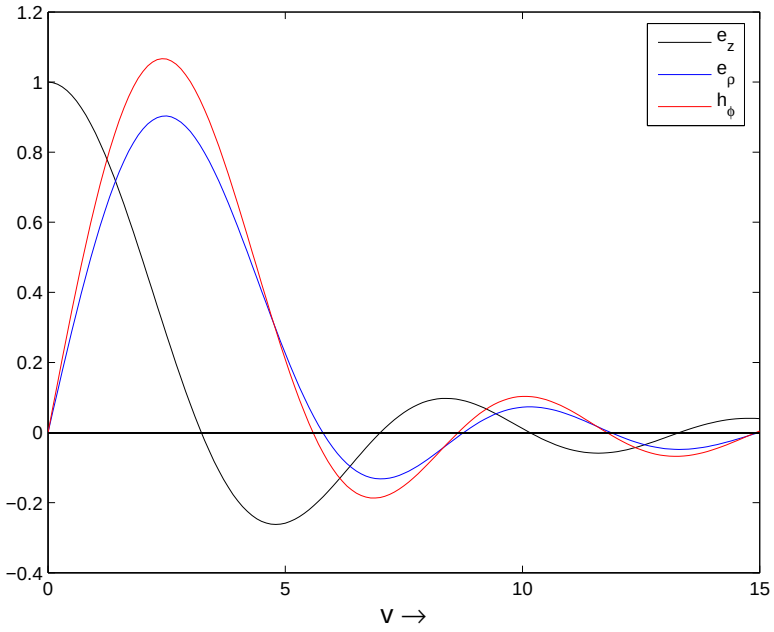

Figure 2.2: Illustration of the stable singularities of the electromagnetic field for $\alpha = \pi/4$ and $\beta = 1$. The magnitudes of e_ρ, e_z, and h_ϕ are shown. All three components are normalized by $\Im\{e_z(0,0)\}$.

For a radially polarized field, all three components possess singularities in the focal plane ($u = 0$). These manifest themselves as Airy-like rings. In the focal plane, h_ϕ and e_ρ are purely real and e_z is purely imaginary. In Fig. 2.2, the real scalars $h_\phi(0,v)$, $e_\rho(0,v)$ and $\Im\{e_z(0,v)\}$ are shown. The zero crossing of each line represents a stable singularity of that component. Technically, these singularities are unstable in the sense that an aberration of the lens can cause them to annihilate, as can a perturbation of the input field, but since these are not system parameters in this thesis, these rings will exist for all values of α and β.

It should be noted that, while e_z is nonzero along the optical axis ($v = 0$), both e_ρ and h_ϕ are zero. The optical axis is, in fact, a stable singular *line* for these two components. The previously mentioned singularities all have their basis in a symmetry of the system. Non-aberrated focusing has certain symmetry properties about the focal plane (see Sec. 3.1).

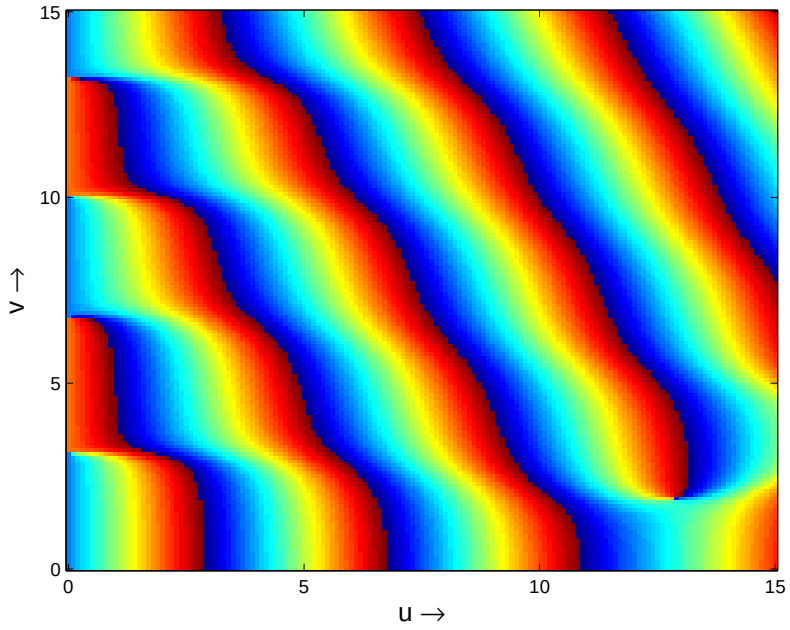

Figure 2.3: The phase of $e_z(u, v)$ for $\alpha = \pi/4$ and $\beta = 1$.

Also, the $\hat{\rho}$ and $\hat{\phi}$ directions are undefined when $\rho = 0$. These symmetry properties are the at the root of these singularities.

There are, however, phase singularities that are not based only on symmetry arguments. Figures 2.3-2.5 show the phase of each component. Although the three images are quite similar, there are notable differences in the location of the singularities along $u = 0$ and the location of the off-axis singularities, identifiable by the swirling of phase around them. The h_ϕ and e_ρ components are remarkably similar, which is not surprising given the form of Eq. (2.9) and Eq. (2.13).

It is important to note at this point that these figures are two-dimensional mappings of three-dimensional fields. The singular points are, in fact, rings. Consider, for example, the singular point in Fig. 2.3 at $(u, v) = (12.5, 2.5)$. The total phase-field for the e_z component can be thought of as a rotation of this figure about the optical axis. Consider, now, a plane $y = 0$ cutting through the field. There will now be two singularities - one at $(u, x') = (12.5, 2.5)$ and another at $(12.5, -2.5)$. Notice the change from v to x', where $x' = x \sin\alpha$ in the original coordinate system. These singularities have *opposite* charge! As the system

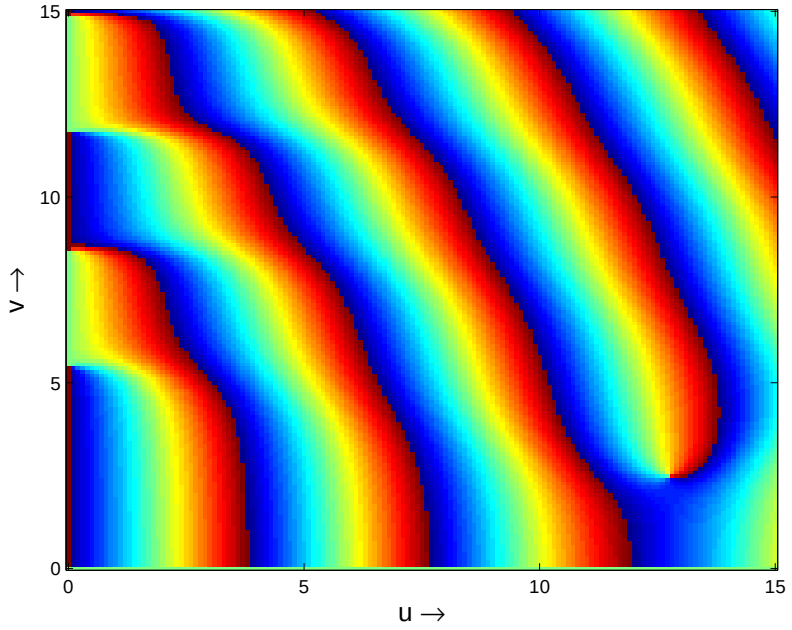

Figure 2.4: The phase of $e_\rho(u, v)$ for $\alpha = \pi/4$ and $\beta = 1$.

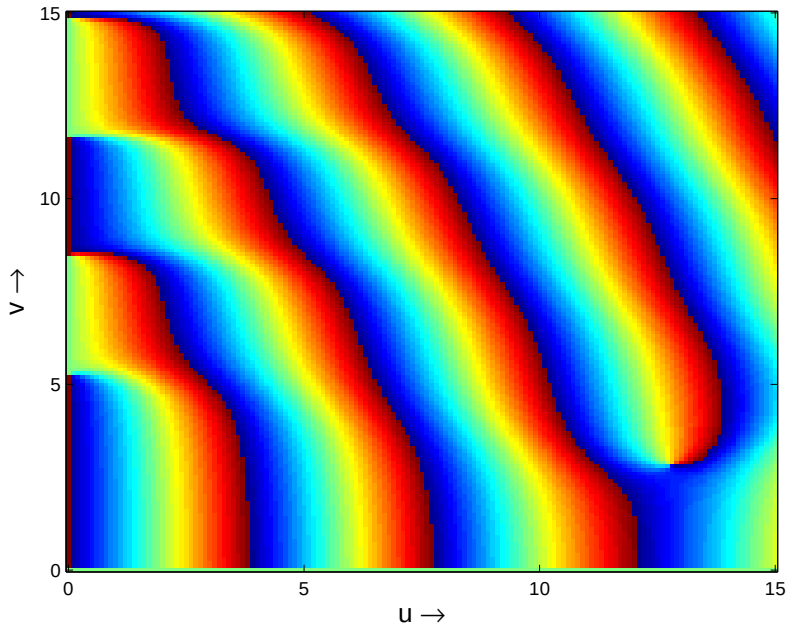

Figure 2.5: The phase of $h_\phi(u, v)$ for $\alpha = \pi/4$ and $\beta = 1$.

parameter α is increased, this ring will shrink around the optical axis. As the radius goes to zero, these singularities will annihilate pair-wise across the optical axis, thus conserving charge. What appeared to be one singularity was actually an infinite number of them formed in a ring with zero cumulative charge. Movies of these ring annihilations can be found online [14].

There can also be unstable, nongeneric singularities in a wavefield. Because of the high degree of symmetry in this focusing problem, they do not appear in the scalar fields. However, as will be shown in Ch. 3, unstable, higher order singularities do exist.

An exhaustive cataloging of the various locations and annihilation events of singularities for these three components is beyond the scope of this thesis. Rather, the phase singularities were introduced and briefly commented on so that they are recognizable in the final chapters when the interrelation between these field components is discussed.

CHAPTER 3

POLARIZATION SINGULARITIES

The standard description of the state of polarization in terms of Stokes parameters [16] applies to plane waves, i.e., to fields in which the electric field only has two nonzero Cartesian components, both perpendicular to the direction of propagation. On focusing a plane wave, the electric field acquires a third nonzero component which is directed along the direction of propagation (the so-called longitudinal field component) [27]. Under the assumption of paraxiality (i.e., assuming the semiaperture angle of the focusing system to be small), this third component may be neglected. The configuration examined in this thesis is not a paraxial one, but in cylindrical coordinates only two components of the electric field are nonzero. This means that with a suitable change in the definition of the Stokes parameters, the usual description of the state of polarization and, in particular, of polarization singularities can be applied.

3.1 The State of Polarization

The electric field in the focal region is given by the formula

$$\mathbf{e}(u,v) = e_z(u,v)\hat{\mathbf{z}} + e_\rho(u,v)\hat{\boldsymbol{\rho}}, \tag{3.1}$$

with the components $e_z(u,v)$ and $e_\rho(u,v)$ given by Eqs. (2.8) and (2.9), and with $\hat{\mathbf{z}}$ and $\hat{\boldsymbol{\rho}}$ unit vectors in the longitudinal and radial direction, respectively. Defining the variables

$$a_1 = |e_z(u,v)|\,, \tag{3.2}$$

$$\delta_1 = \arg[e_z(u,v)], \tag{3.3}$$

$$a_2 = |e_\rho(u,v)|\,, \tag{3.4}$$

$$\delta_2 = \arg[e_\rho(u,v)], \tag{3.5}$$

the state of polarization of the field may then be characterized by the four Stokes parameters (cf. [16, Sec. 1.4] for a similar definition with respect to a Cartesian coordinate system):

$$S_0 = a_1^2 + a_2^2, \tag{3.6}$$

$$S_1 = a_1^2 - a_2^2, \tag{3.7}$$

$$S_2 = 2a_1 a_2 \cos\delta, \tag{3.8}$$

$$S_3 = 2a_1 a_2 \sin\delta, \tag{3.9}$$

with the phase difference δ given by

$$\delta = \delta_2 - \delta_1. \tag{3.10}$$

For any given intensity (i.e., $S_0 = \text{constant}$), the normalized Stokes parameters $s_i = S_i/S_0$ may be represented as a point on the Poincaré sphere (see Fig. 3.1). On the north pole ($s_1 = s_2 = 0, s_3 = 1$), the polarization is circular. We adopt the convention of calling this state right-handed because, according to Eq. (2.1), the ellipse is being traversed in a clockwise manner in the (e_z, e_ρ)-plane. The polarization is right-handed for points on the northern hemisphere, and left-handed on the southern hemisphere. It easily verified that at the south pole ($s_1 = s_2 = 0, s_3 = -1$), the polarization is circular and left-handed. For all points on the equator ($s_3 = 0$), the polarization is linear. At ($s_1 = 1$, $s_2 = s_3 = 0$) the field is purely z-polarized, whereas at ($s_1 = -1$, $s_2 = s_3 = 0$) it is purely ρ-polarized. At ($s_1 = 0, s_2 = 1, s_3 = 0$) and ($s_1 = 0, s_2 = -1, s_3 = 0$), finally, the linear polarization is under angle of $+\pi/4$ and $-\pi/4$ in the (e_z, e_ρ)-plane, respectively. For the case that $a_1 \geq a_2$, the orientation of the ellipse is described by the angle ψ between the major semiaxis and the

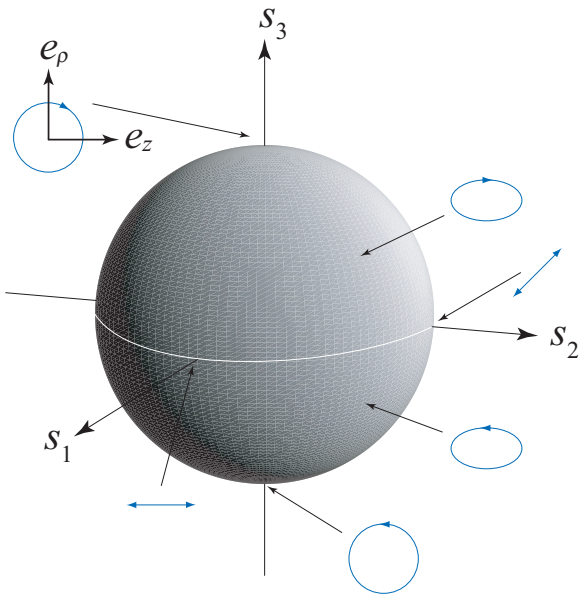

Figure 3.1: The Poincaré sphere with cartesian axes (s_1, s_2, s_3).

z-direction. It is given by the expression [16, Sec. 1.4.2, Eq. (46)]

$$\psi = \frac{1}{2}\tan^{-1}\left(\frac{s_2}{s_1}\right). \tag{3.11}$$

It follows from Eqs. (2.8) and (2.9) that at any two points (u, v) and $(-u, v)$ that are symmetrically located with respect to the focal plane, the field components satisfy the symmetry relations

$$e_z(-u, v) = -e_z^*(u, v), \tag{3.12}$$

$$e_\rho(-u, v) = e_\rho^*(u, v), \tag{3.13}$$

where the asterisk denotes complex conjugation. Clearly, the variables a_1 and a_2 remain unchanged under reflection of the point of observation in the focal plane. The behavior of the other quantities that describe the state of polarization is summarized in Table 3.1. The antisymmetrical behavior of the second Stokes parameter and the angle ψ implies that they both vanish identically in the focal plane, i.e.,

$$s_2(0, v) = 0; \quad \psi(0, v) = 0. \tag{3.14}$$

The symmetry properties of the polarization ellipse are illustrated in Fig. 3.2. If, for example,

Table 3.1: The behavior of various quantities that characterize the state of polarization under reflection of the point of observation in the focal plane.

(u,v)	δ_1	δ_2	δ	s_0	s_1	s_2	s_3	ψ
(-u,v)	$\pi - \delta_1$	$-\delta_2$	$-\delta - \pi$	s_0	s_1	$-s_2$	s_3	$-\psi$

the major semiaxis of the polarization ellipse at a point (z, x) makes an angle ψ with the positive z-axis, then at a point $(-z, x)$ the orientation angle will be $-\psi$. The handedness, however, is the same at both positions. The orientation of the ellipse and its handedness at $(z, -x)$ and $(-z, -x)$ follow from considering the rotational symmetry of the field.

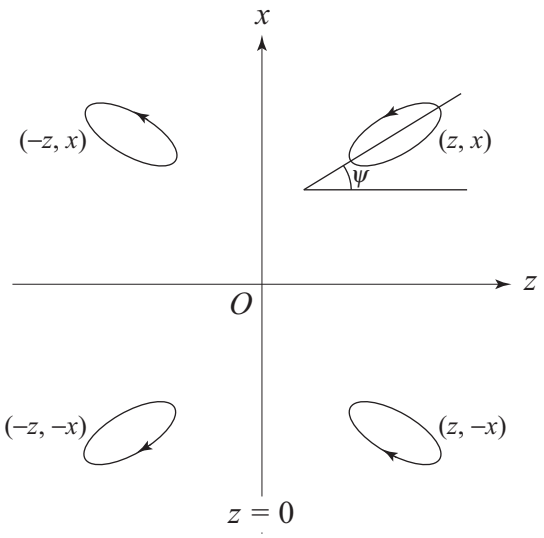

Figure 3.2: Illustrating the symmetry properties of the polarization ellipse.

3.2 Polarization Singularities

At points where the polarization ellipse degenerates into a circle or into a line, the polarization is said to be singular. At C-points (i.e., $s_3 = \pm 1$), where the polarization is circular, the orientation angle ψ of the ellipse, as given by Eq. (3.11), is undetermined. At C-points the polarization can either be left-handed or right-handed. At L-lines (i.e., $s_3 = 0$), where the polarization is linear, the handedness of the ellipse is undetermined. In the remainder of

this chapter, these two types of polarization singularities are examined. It should be noted that, because of rotational symmetry, points and closed lines in the (u, v)-plane are circles and tori, respectively, in three-dimensional space.

3.2.1 Linear polarization

It follows from Eq. (3.9) that linear polarization generically occurs at points (u, v) at which

$$\Re\{e_z(u,v)\} * \Im\{e_\rho(u,v)\} = \Im\{e_z(u,v)\} * \Re\{e_\rho(u,v)\}. \tag{3.15}$$

This single condition is typically satisfied on a line in (u, v)-space. A subset of these points consists of locations where one of the two field components is zero, i.e., at phase singularities of either field component. For example, for the longitudinal component these occur at points at which

$$\Re\{e_z(u,v)\} = \Im\{e_z(u,v)\} = 0. \tag{3.16}$$

These two conditions are typically satisfied at isolated points in (u, v)-space. Phase singularities of both field components are found in the focal plane and at other points in space. They can be created or annihilated by smoothly varying the width of the incident beam or the semiaperture angle [14].

By drawing the contours of $s_3 = 0$, a multitude of L-surfaces is found. As can be seen in Fig. 3.3, the phase singularities of the two electric field components all lie on L-surfaces. Notice that there is a surface of linear polarization that connects each Airy ring of e_z in the focal plane to the adjacent Airy ring of e_ρ. On traversing these closed surfaces in the (u, v)-plane, the Stokes vector makes a complete rotatation along the equator of the Poincaré sphere.

It is seen from Eq. (2.9) that on the central axis (i.e., $v = 0$) the radial electric field component vanishes. Therefore this axis constitutes an L-line. It follows from rotational symmetry that its index is $+1$ (see [2, Sec. 13.3]).

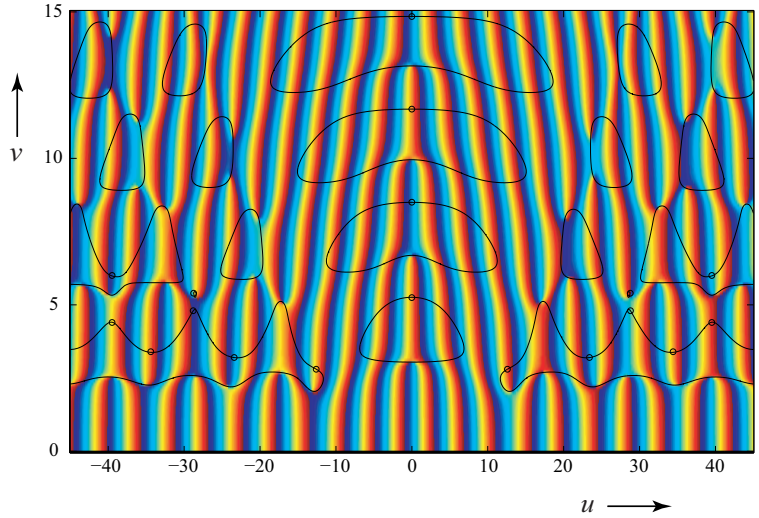

Figure 3.3: The loci of linear polarization, i.e., contours of $s_3 = 0$, in the focal region. Because of the rotational symmetry of the field, these are tori centered on the u-axis. The contours are superposed on a color-coded phase map of e_z. Phase singularities of e_z are located at points where all different colors converge. The open circles indicate phase singularities of the other field component, e_ρ. In this example $\alpha = \pi/4$ and $\beta = 0.5$.

3.2.2 Circular polarization

It follows from the definitions (3.7)–(3.9) that circular polarization generically occurs at points rather than lines in the (u, v)-plane. One way of locating C-points is to represent the field in a circular polarization basis (cf. [28] for an similar decomposition in cartesian coordinates), i.e.,

$$\mathbf{e}(u, v) = e_+(u, v)\hat{\mathbf{c}}_+(u, v) + e_-(u, v)\hat{\mathbf{c}}_-(u, v), \tag{3.17}$$

where

$$e_\pm = (e_z \mp \mathrm{i}e_\rho)/\sqrt{2}, \qquad \hat{\mathbf{c}}_\pm = (\hat{z} \pm \mathrm{i}\hat{\rho})/\sqrt{2}. \tag{3.18}$$

Thus e_+ (e_-) represents the amplitude of the right- (left-) handed circular component of the field. In this way, C-points correspond to phase singularities of either circular component. An example is presented in Fig. 3.4. It is seen that the number of right- and left-handed C-points is approximately the same. However, there is a line (a cylindrical sheet in three-

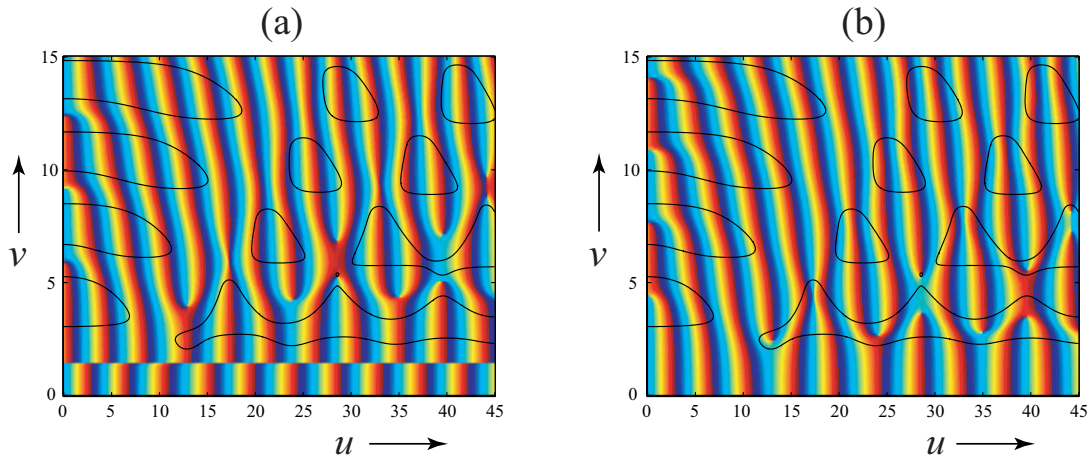

Figure 3.4: A color-coded phase map of (a) e_+ and (b) e_-, both with lines of linear polarization (solid black curves) superposed. Left-handed C-points are phase singularities of e_+ in panel (a), whereas right-handed C-points are singularities of e_- in panel (b). In this example $\beta = 0.5$ and $\alpha = \pi/4$.

dimensional space) of left-handed circular polarization at approximately $v = 1.4$. This is a nongeneric surface that appears to be only weakly dependent on the parameters u and β. To understand this feature more fully, it is instructive to apply a Taylor expansion in θ to Eqs. (2.8) and (2.9). These expressions then become

$$e_z(u,v) = -\mathrm{i}kf^2 \int_0^\alpha \theta^3(1-\beta^2\theta^2)\exp(\mathrm{i}u/\sin^2\alpha)\,\mathrm{d}\theta, \tag{3.19}$$

$$e_\rho(u,v) = -kf^2 \int_0^\alpha \theta^3(1-\beta^2\theta^2)\exp(\mathrm{i}u/\sin^2\alpha)\frac{v}{2\sin\alpha}\,\mathrm{d}\theta. \tag{3.20}$$

Thus, e_+ can be written as

$$e_+(u,v) = -\frac{\mathrm{i}kf^2}{\sqrt{2}}\exp(\mathrm{i}u/\sin^2\alpha)\left[1-\frac{v}{2\sin\alpha}\right]\int_0^\alpha \theta^3(1-\beta^2\theta^2)\,\mathrm{d}\theta. \tag{3.21}$$

It is readily apparent that left-handed circular polarization occurs when $v = 2\sin\alpha$. Also, because the zero of e_+ is independent of the longitudinal variable u, this phase singularity is line-shaped. Notice that there is no corresponding C-surface for right-handed circular polarization because the resulting equation would yield (at first order) $v = -2\sin\alpha$, whereas v is positive definite. To test the validity of this approximation, the computed location of the C-surface is compared to the approximate values in Table 3.2. Even when the semiaperture angle $\alpha = 60°$, the approximation is seen to hold quite well.

Apart from their handedness, C-points can be classified into three distinct types based on the local behavior of the polarization ellipses (see [2, Secs. 4.10 and 12.2] and Ref. [29]). These types are *stars* (with index $-1/2$), *monstars* (index $1/2$), and *lemons* (index $1/2$). This local behavior is shown in Fig. 3.5 for the pair of C-points seen in Fig. 3.4 (b) near $(u, v) \approx (28, 5)$ for three different values of the semiaperture angle α. Indicated in red are the local straight-line orientations of the major axis of the nearby ellipses (a single line for lemons, and three lines for stars and monstars). In Fig. 3.5(a) both a star (top) and a lemon (bottom) can be seen. The lemon-type polarization singularity has evolved into a monstar in Fig. 3.5(b). In Fig. 3.5 (c) the situation is shown after the star and the monstar have annihilated.

3.2.3 Relationship between L-lines and C-points

There is a strong connection between L-lines and C-points. The former separate space into regions of different handedness. In agreement with this, the left-handed C-points in Fig. 3.4 (a) are all located outside the closed L-lines, whereas the right-handed C-points in Fig. 3.4 (b) are all located within them. As reported by Freund et al. [19], there is a relation between the charge of component singularities on a closed L-line and the total charge of C-points enclosed by it. For this specific case Eq. (5) of [19] can be rewritten (see Appendix A.1) as

$$2 \sum_{\in L} q_{-} = \sum_{L} q_{\rho} + \sum_{L} q_{z}, \tag{3.22}$$

Table 3.2: Comparison of the approximate location of the C-surface to its actual location. In these examples $\beta = 0.5$.

α	actual v	$v = 2 \sin \alpha$	Error
15°	0.515	0.517	0.50%
30°	1.005	1.000	0.50%
45°	1.425	1.414	0.76%
60°	1.765	1.732	1.87%

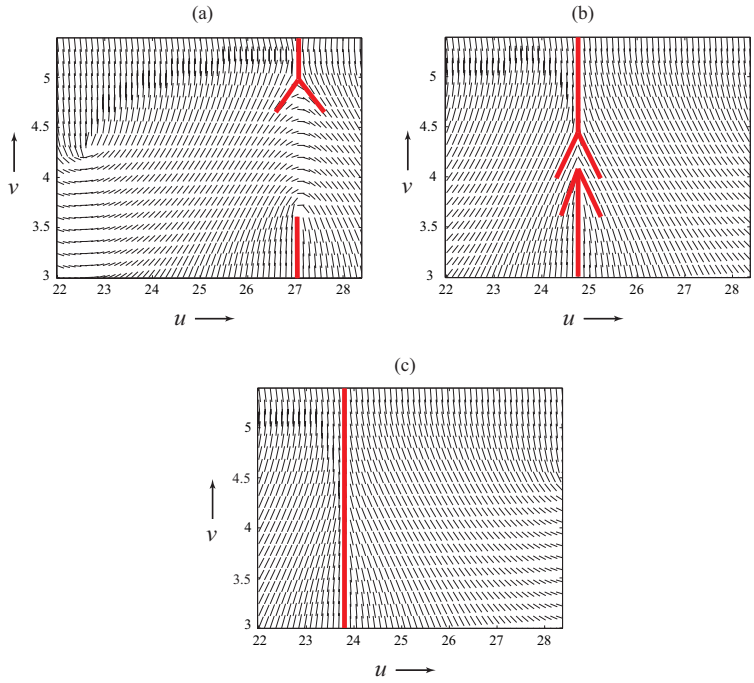

Figure 3.5: Local orientation of the major axis of the electric polarization ellipse shown for three different values of the semiaperture angle α with the beam parameter β kept fixed at 0.5. The local straight-line orientations of the major axes are shown in red. In panel (a) ($\alpha = 52°$), a star (above) and a lemon (below) are seen. In panel (b) ($\alpha = 61°$), the lemon has transitioned into a monstar. In panel (c) ($\alpha = 65°$), the annihilation leaves only a straight-line orientation of the major axis.

where the summation on the left-hand side is over all topological charges of C-points enclosed by the L-line, and the right-hand summations are over the charges of the two electric field components on the L-line. For example, it was verified that the two L-lines that contain the points $(0, 4)$ and $(22, 7)$ in Figs. 3.3 and 3.4 both satisfy this sum rule.

Figure 3.6 is the first in a series of figures that show the evolution of the left-handed field component e_- and the L-lines as the semiaperture angle α is increased. The whole series of figures can be seen online [15]. In that series, the L-lines deform, separate, and merge. A small L-line that contains a C-point in its interior can be seen to break off when $\alpha \approx 43°$, and unite with another L-line when $\alpha \approx 46.5°$. In addition, a C-point annihilation is seen near $\alpha \approx 61°$. The upper singularity is a star and the lower singularity is a lemon that evolves

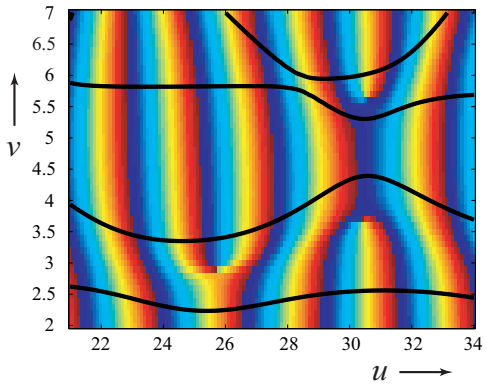

Figure 3.6: A color-coded phase map of the left-handed component e_- with L-lines, shown in black, superposed. The semiaperture angle α is 35° and β is 0.5.

into a monstar before the annihilation takes place. Figure 3.5 shows the corresponding local ellipse behavior for this event.

3.2.4 Vector singularities

In addition to the different kinds of singularities mentioned in Ch. 1, there exist also points where the two-dimensional complex electric vector field $\mathbf{e}$ is identically zero. Such points are referred to as V-points [30]. V-points are necessarily a phase singularity of both cylindrical components and of both components in the circular polarization basis. They are to be distinguished from singularities of real-valued vector fields such as the Poynting vector [5]-[7]. Since the complex electric field given by Eqs. (2.8) and (2.9) is an analytic function, its zeros are isolated points in the (u, v) plane [31]. Because the condition $\mathbf{e}(u, v) = 0$ has codimension four, V-points do not generically occur. However, as will be demonstrated, they do appear in the focal region of radially polarized beams.

In this configuration V-points occur, for example, when the longitudinal component e_z is zero on the optical axis (where the radial component e_ρ is identically zero). In Fig. 3.7 the real and imaginary parts of e_z are shown. In a movie located online [15] their intersection near $u = 11.5$ is seen to move towards and eventually below the horizontal axis when the semiaperture angle α is increased in a continuous manner. At approximately $\alpha = 56.6°$,

this intersection crosses the horizontal axis, i.e., $\Re\{e_z\} = \Im\{e_z\} = 0$ near $(u, v) = (11.5, 0)$. Clearly this V-point is unstable under perturbations.

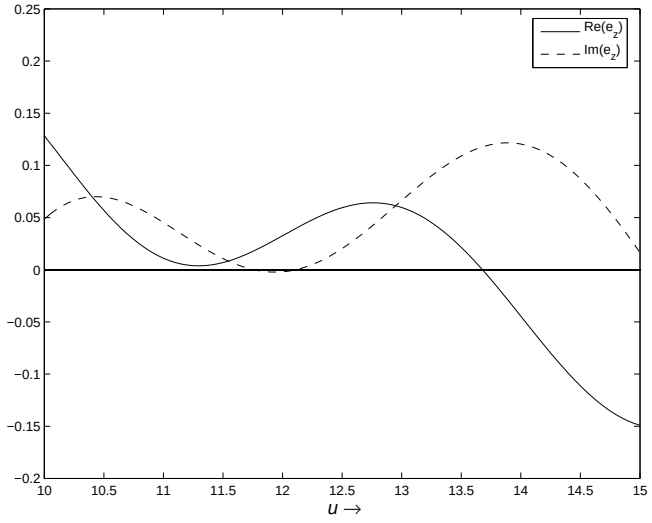

Figure 3.7: The real and imaginary parts of e_z along the optical axis normalized to $\Im\{e_z(0,0)\}$. In this frame, $\alpha = 55.0°$ and $\beta = 1.5$.

Another way in which vector singularities may occur is through the collision of an L-line and a C-point [17]. Although the field at a V-point is neither linearly nor circularly polarized, the condition for linear polarization ($S_3 = 0$) combined with the two conditions for circular polarization ($S_1 = S_2 = 0$) results in the necessary condition that $S_0 = 0$; i.e., the electric field vanishes at the collision point. An example of such an event is shown in Appendix B in which the semiaperture angle α is gradually increased. In the upper frames, the L-line that is seen to break apart moves downwards towards the horizontal C-line near $v = 1.6$. In this process, shown in the lower frames, the L-line shrinks and collapses to a point at the moment of collision. On further increasing α, this point changes back into an L-line that approaches the optical axis. The C-line remains essentially stationary while the L-line passes through it. A movie of this annihilation is found in [15].

It is worth mentioning that the L-line of interest in Fig. 3.8 intersects one phase singularity of each cylindrical component and encloses one point of pure right-handed circular polarization. When the L-line collapses to a point at the line of pure left-handed polarization (at approximately $v = 1.6$), both cylindrical singularities coincide, creating a V-point.

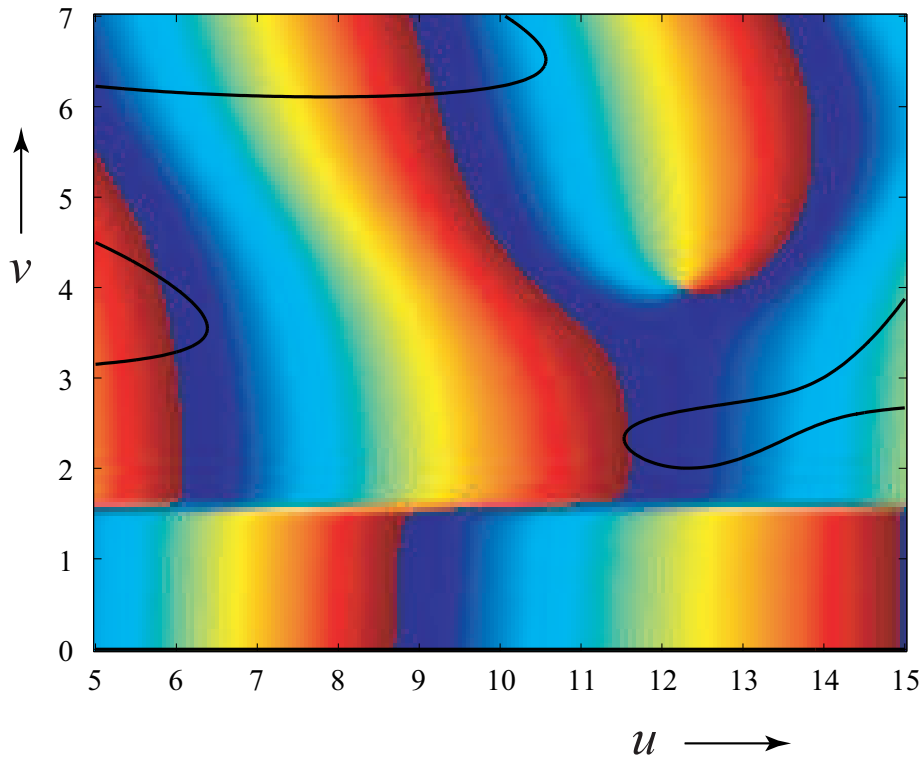

Figure 3.8: A color-coded phase map of e_+ with L-lines (solid black curves) superposed with the semiaperture angle $\alpha = 50.0°$ and with β kept fixed at 1.5.

Alternatively, the V-point can be be considered as the collision of phase singularities of the circular components e_+ and e_-. In fact, because L-surfaces separate space into regions of right- and left-handedness, the only way in which C-points of opposite handedness can collide is when the L-line separating them collapses to a point.

CHAPTER 4

THE POYNTING VECTOR

Singularities of the Poynting vector have been studied previously [5, 6, 7]. In these studies, a two-dimensional geometry is assumed and the analysis is separated into TE and TM polarizations. The Poynting vector is then written in terms of the transverse field component only. Analogously, radially symmetric, focused fields can be separated into a TE and TM basis, where the transverse-like component is the azimuthal one. Thus, radially polarized electric fields are TM. Likewise, for an azimuthally polarized electric field, knowledge of the electric field alone defines the system after focusing.

As shown in Appendix A.2, the Poynting vector for a focused radially polarized field is given by

$$< \mathbf{S}(\rho, z) >= \frac{c}{8\pi\epsilon k}|h_\phi(\rho, z)|^2 \nabla\psi_h(\rho, z). \tag{4.1}$$

Likewise, the Poynting vector for a focused, azimuthally polarized field is given by

$$< \mathbf{S}(\rho, z) >= \frac{c}{8\pi\mu k}|e_\phi(\rho, z)|^2 \nabla\psi_e(\rho, z). \tag{4.2}$$

An angle, Θ, that serves to define the direction of the Poynting vector with respect to the z-direction (the direction of propagation before focusing), is given by

$$\Theta = \tan^{-1}\frac{S_\rho}{S_z}. \tag{4.3}$$

At points where the Poynting vector is zero, this angle is not defined. These are referred to as singular points of the real-valued vector field $< \mathbf{S} >$. These singular points can be separated into two types: points where the magnitude of h_ϕ (e_ϕ) is zero and points where the gradient of the phase of h_ϕ (e_ϕ) is zero. The latter type are referred to as stationary

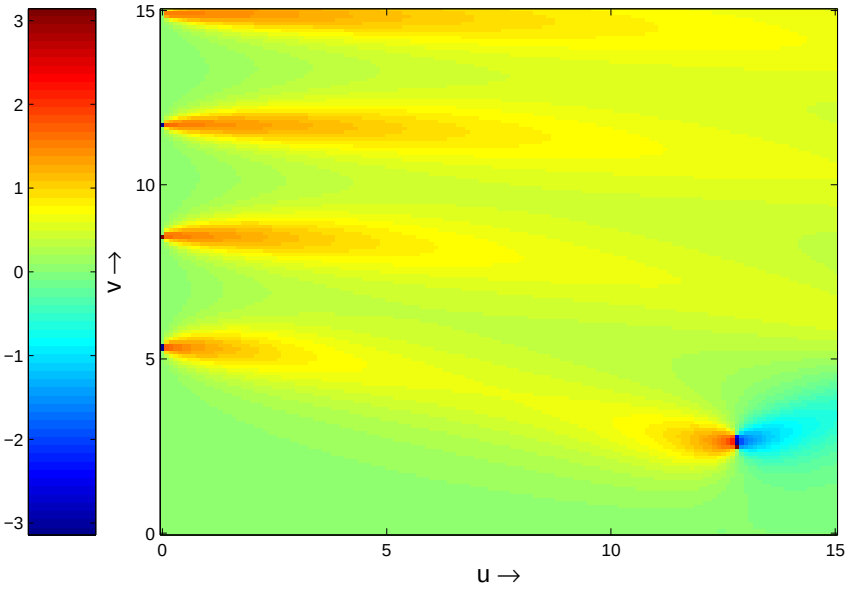

Figure 4.1: Θ for $\alpha = \pi/4$ and $\beta = 1$.

points of the phase, whereas the former are the phase singularities of previous chapters. More importantly, the type of field component singularity associated with the power flow singularity can easily be deduced. A left-circulating phase singularity of h_ϕ corresponds to a left-circulating singularity of $< \mathbf{S} >$, and likewise for a right-circulating phase singularity. Phase saddles (the only type of stationary point found in this system) of h_ϕ correspond to power flow saddles.

In Fig. 4.1, the angle $\Theta(u, v)$ is displayed. The fact that Θ is generally around zero implies that the Poynting vector mostly points in the positive u-direction, as one would expect. There are six singularities present in this figure: four are in the focal plane and correspond to the Airy-like rings discussed in Sec. 2.2; two more are around $(u, v) = (12.5, 2.5)$. The upper of these two is associated with a phase singularity of the magnetic field (see Fig. 2.5) and the lower with a phase saddle. This can be more easily seen in Fig. 4.2.

As one would expect from the definition of the Poynting vector [see Eq. (A.12)], V-points correspond to power flow singularities just as zeros of the magnetic field (phase singularities of h_ϕ) do. More specifically, V-points correspond to power flow saddles. However, as was

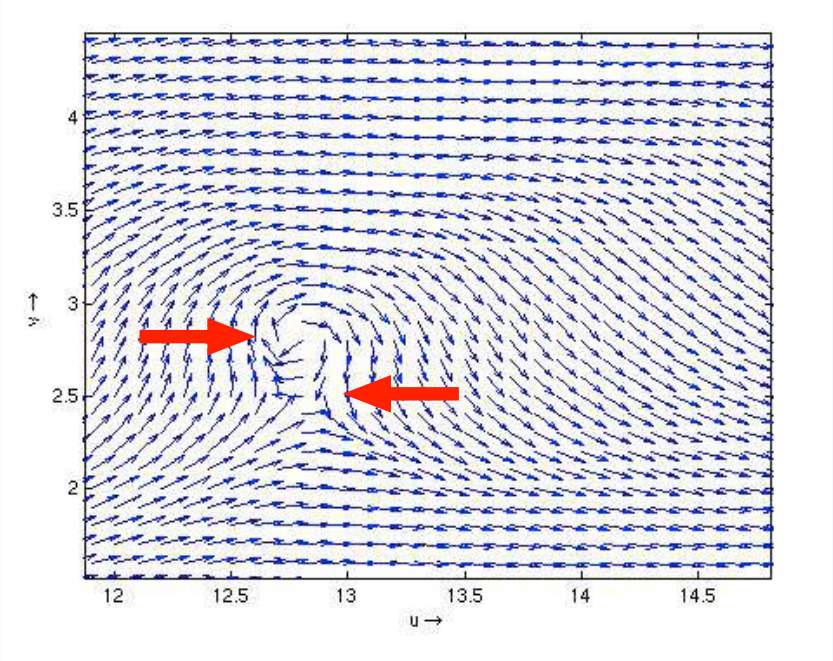

Figure 4.2: Direction lines of $< \mathbf{S} >$ for $\alpha = \pi/4$ and $\beta = 1$. The upper arrow points to a point of power flow circulation and the lower arrow points to a power flow saddle.

pointed out in Sec. 3.2.4, V-points are quite rare, whereas power flow saddles are not. Points where there is a power flow saddle are not necessarily V-points. As a system parameter is smoothly changed, a power flow saddle can momentarily correspond to a V-point. The rest of the time, the phase saddle merely corresponds to a point where both electric field components are 90° out of phase with the azimuthal magnetic field component, which is the most general condition for the Poynting vector to be zero.

CHAPTER 5

CONCLUSION

This thesis represents a thorough analysis of focused, radially symmetric fields through the tools of singular optics. Each field component was briefly analyzed separately using scalar, singular optics methods. The electric field, however, is not amenable to a scalar treatment and was analyzed more fully with the help of the Stokes parameters. A variety of different singularities were seen to exist: lines and surfaces of linear polarization, lines and a single surface of circular polarization, and lines and points of zero electric field. It was shown how these types of singularities interact as a system parameter was changed. Finally, the Poynting vector was introduced and analyzed, and certain relationships between previously discussed singular points and the singularities of the Poynting vector were examined.

Although the analysis in this thesis was specific to radially polarized fields, the method can be used to consider any type of field one wishes. However, the high degree of symmetry in radially polarized fields allows for the use of a modified form of paraxial singular optics (polarization singularities) to study the electric field and scalar singular optics to study the magnetic field. More involved calculations are needed to analyze fields without this symmetry and much work still needs to be done to formulate a framework for analyzing all the singular points in an electromagnetic field.

APPENDIX A

MATHEMATICAL DERIVATIONS

A.1 The Sign Rule

The general sign rule, as written in [19], is

$$2\sigma_k \sum_{(k)} q_{ij} = \sum^{(k)} \sigma_i q_{jk}, \tag{A.1}$$

where $\sum_{(k)}$ is used to denote the sum of singularities enclosed by the line Z_k (level curves $S_k = 0$) and $\sum^{(k)}$ is used to denote the sum of singularities on the line Z_k. Also, σ_i =sign(S_i) and q_{ij} is the topological charge of a singularity of the Stokes scalar $S_{ij} = S_i + \mathrm{iS_j}$. In looking for the relationship between L-lines and C-points, only $k = 3$ (L-lines) are of importance. In the configuration specific to this class of problems, L-lines enclose only right-handed circular points (singularities of e_-); therefore, $\sigma_3 = 1$. Equation (A.1) then simplifies to

$$2 \sum_{\in L} q_{12} = \sum_{L} \sigma_1 q_{23}. \tag{A.2}$$

By rewriting the Stokes parameters from Eqs. (3.7)-(3.9)

$$S_1 = |e_z|^2 - |e_\rho|^2, \tag{A.3}$$

$$S_2 = 2\Re\{e_z^* e_\rho\}, \tag{A.4}$$

$$S_3 = 2\Im\{e_z^* e_\rho\}, \tag{A.5}$$

it is obvious that $\sigma_1 = 1$ for singularities of e_ρ and $\sigma_1 = -1$ for singularities of e_z. Also, it is readily apparent that $S_{23} = 2e_z^* e_\rho$. Thus, $q_{23} = q_\rho$ when the singularity is in e_ρ and $q_{23} = -q_z$

when the singularity is in e_z. Finally, it is necessary to find the relationship between q_{12} and singularities in e_-. By writing

$$e_\rho = \frac{e_- - e_+}{\mathrm{i}\sqrt{2}}, \tag{A.6}$$

$$e_z = \frac{e_- + e_+}{\sqrt{2}}, \tag{A.7}$$

and inserting these relations into Eqs. (A.3-A.5) it is seen that

$$S_1 = 2\Re\{e_+^* e_-\}, \tag{A.8}$$

$$S_2 = 2\Im\{e_+^* e_-\}, \tag{A.9}$$

$$S_3 = |e_-|^2 - |e_+|^2, \tag{A.10}$$

and that $S_{12} = 2e_+^* e_-$. Therefore, $q_{12} = q_-$ when the singularity is in e_- and the sum rule is

$$2 \sum_{enclosed} q_- = \sum_{on} q_\rho + \sum_{on} q_z. \tag{A.11}$$

A.2 The Poynting Vector for Radially Symmetric Fields

The fields considered in this thesis are all radially symmetric so that there is no ϕ-dependence for any field quantities. From [16, Section 1.4.3 Eq. (56)], the Poynting vector is defined as

$$< \mathbf{S} >= \frac{c}{8\pi}\Re\{\mathbf{E} \times \mathbf{H}^*\}. \tag{A.12}$$

Based on the above equations and the assumption of rotational symmetry, it can be shown with the help of Eqs. (2.10-2.11) that

$$\begin{aligned} \mathbf{H} &= \frac{-\mathrm{i}}{k\mu}\left(\frac{\partial e_\rho}{\partial z} - \frac{\partial e_z}{\partial \rho}\right)\hat{\phi} \\ &= h_\phi \hat{\phi} \end{aligned} \tag{A.13}$$

in cylindrical coordinates. Then, writing $\mathbf{E}$ in terms of only h_ϕ,

$$\mathbf{E} = \frac{\mathrm{i}}{k\epsilon}\left(-\frac{\partial h_\phi}{\partial z}\hat{\rho} + \frac{1}{\rho}\frac{\partial(\rho h_\phi)}{\partial \rho}\hat{z}\right), \tag{A.14}$$

the following simplification can be made:

$$\begin{aligned}\mathbf{E}\times\mathbf{H}^{*} &= \frac{-\mathrm{i}}{k\epsilon}h_{\phi}^{*}\left(\frac{1}{\rho}\frac{\partial(\rho h_{\phi})}{\partial\rho}\hat{\rho}+\frac{\partial h_{\phi}}{\partial z}\hat{z}\right)\\ &= \frac{-\mathrm{i}}{k\epsilon}h_{\phi}^{*}\left(\nabla h_{\phi}+\frac{h_{\phi}}{\rho}\hat{\rho}\right).\end{aligned} \tag{A.15}$$

Upon taking the real part of Eq. (A.15) the Poynting vector for a radially polarized field can be given by

$$<\mathbf{S}>=\frac{c}{8\pi\epsilon k}\Im\{h_{\phi}^{*}\nabla h_{\phi}\}. \tag{A.16}$$

By writing

$$h_{\phi}(\rho,z)=|h_{\phi}(\rho,z)|e^{i\psi_{h}(\rho,z)}, \tag{A.17}$$

and substituting Eq. (A.17) into Eq. (A.16), the Poynting vector may be expressed as

$$<\mathbf{S}>=\frac{c}{8\pi\epsilon k}|h_{\phi}(\rho,z)|^{2}\nabla\psi_{h}(\rho,z). \tag{A.18}$$

Through a similar exercise, the Poynting vector for an azimuthally polarized field can be found in terms of only one field component, i.e.,

$$<\mathbf{S}>=\frac{c}{8\pi\mu k}|e_{\phi}(\rho,z)|^{2}\nabla\psi_{e}(\rho,z). \tag{A.19}$$

APPENDIX B

CREATION OF A V-POINT

Figures B.1-B.65 show the evolution of a C-point as it crosses a C-line. The resultant crossing yields a V-point.

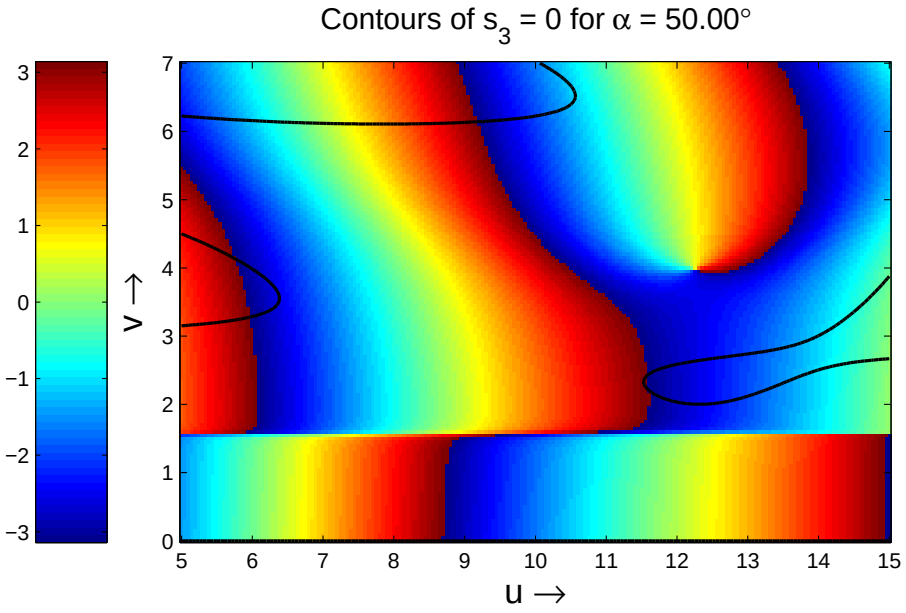

Figure B.1: A color-coded phase map of e_+ with L-lines (solid black curves) superposed and the semiaperture angle 50.00° with β kept fixed at 1.5.

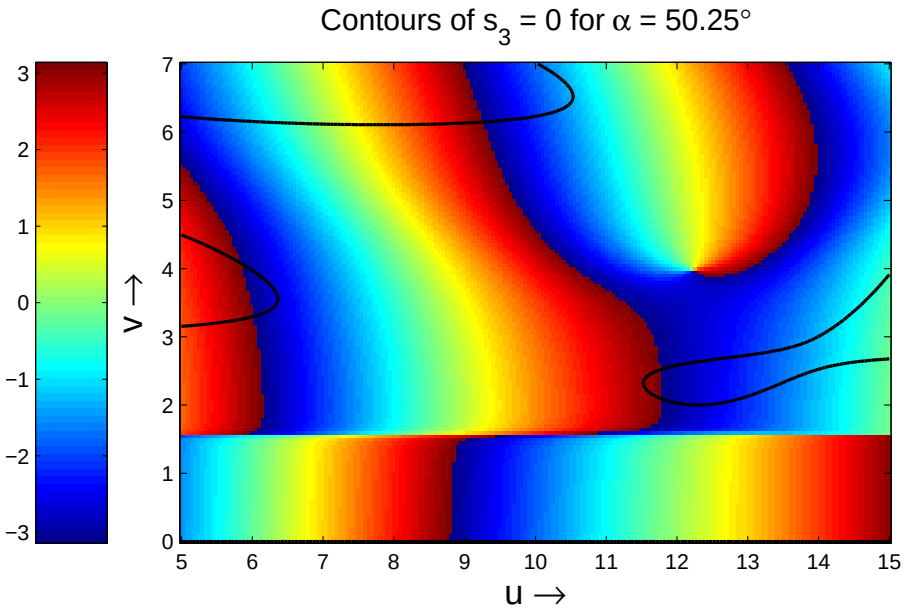

Figure B.2: A color-coded phase map of e_+ with L-lines (solid black curves) superposed and the semiaperture angle 50.25° with β kept fixed at 1.5.

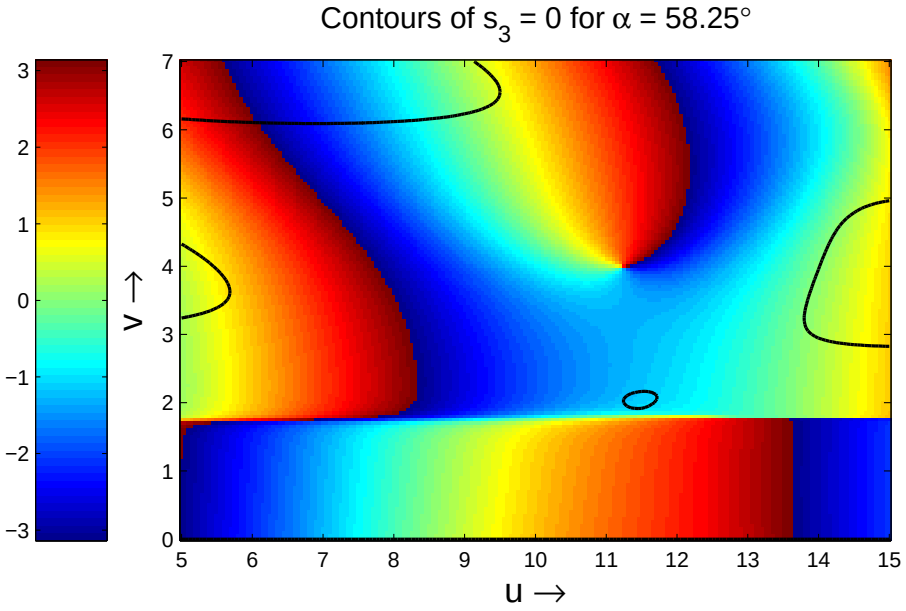

Figure B.3: A color-coded phase map of e_+ with L-lines (solid black curves) superposed and the semiaperture angle 58.25° with β kept fixed at 1.5.

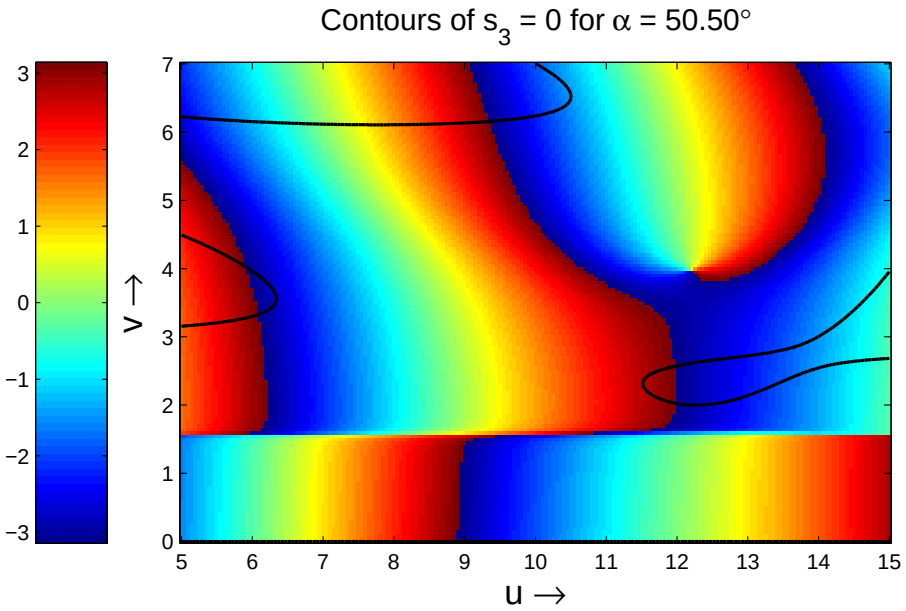

Figure B.4: A color-coded phase map of e_+ with L-lines (solid black curves) superposed and the semiaperture angle 50.50° with β kept fixed at 1.5.

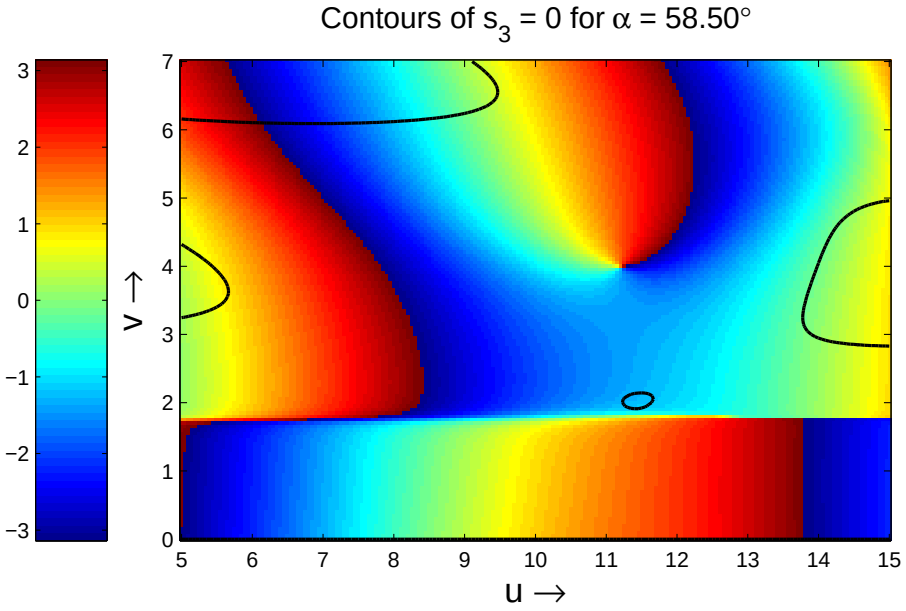

Figure B.5: A color-coded phase map of e_+ with L-lines (solid black curves) superposed and the semiaperture angle 58.50° with β kept fixed at 1.5.

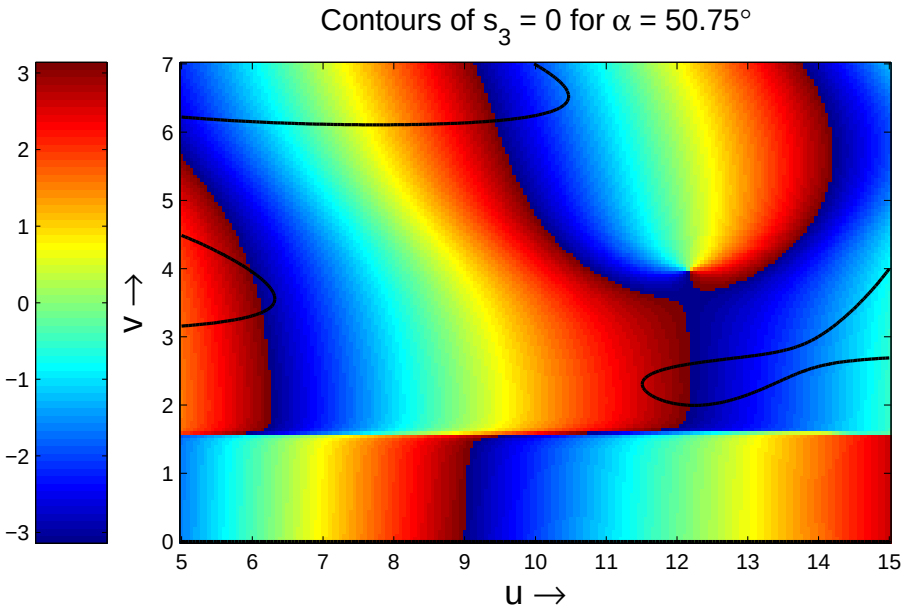

Figure B.6: A color-coded phase map of e_+ with L-lines (solid black curves) superposed and the semiaperture angle 50.75° with β kept fixed at 1.5.

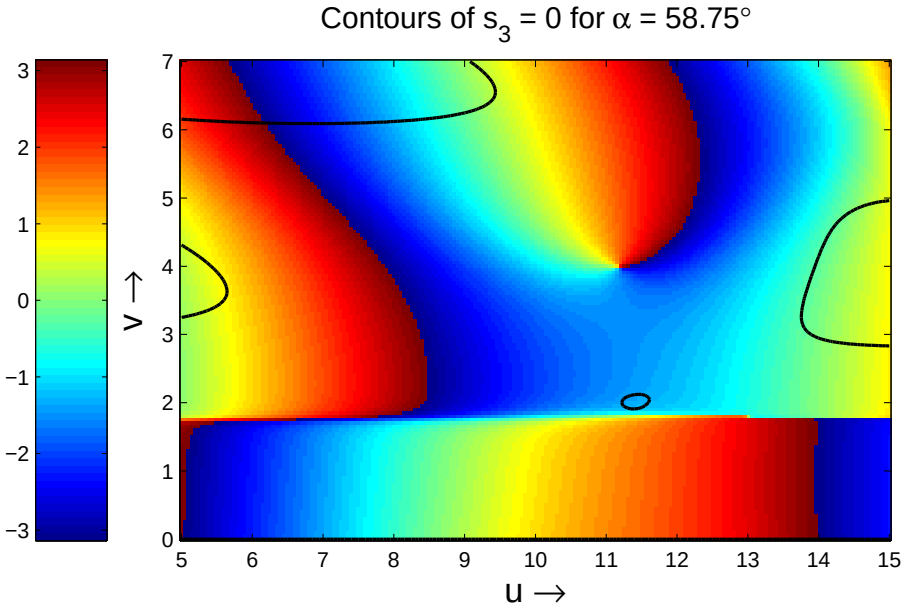

Figure B.7: A color-coded phase map of e_+ with L-lines (solid black curves) superposed and the semiaperture angle 58.75° with β kept fixed at 1.5.

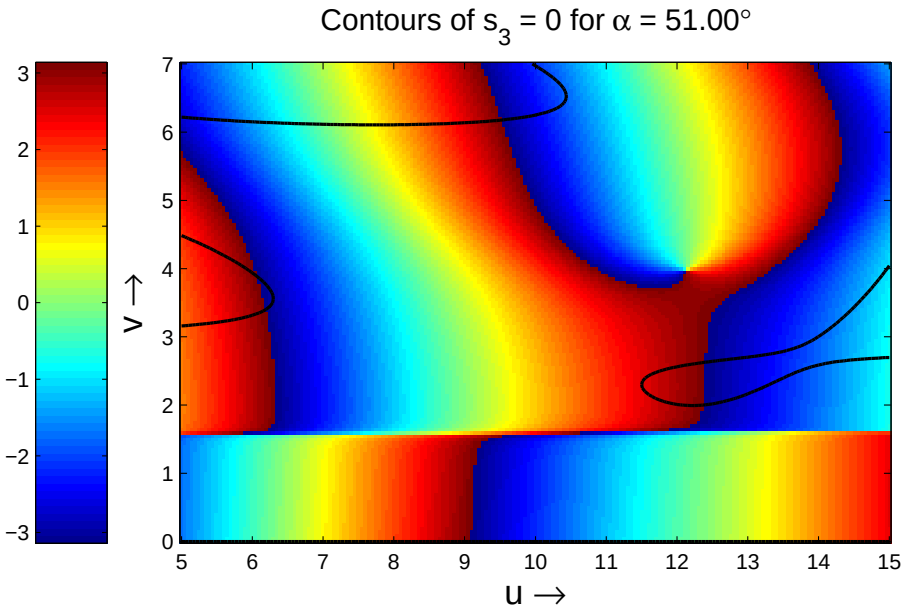

Figure B.8: A color-coded phase map of e_+ with L-lines (solid black curves) superposed and the semiaperture angle 51.00° with β kept fixed at 1.5.

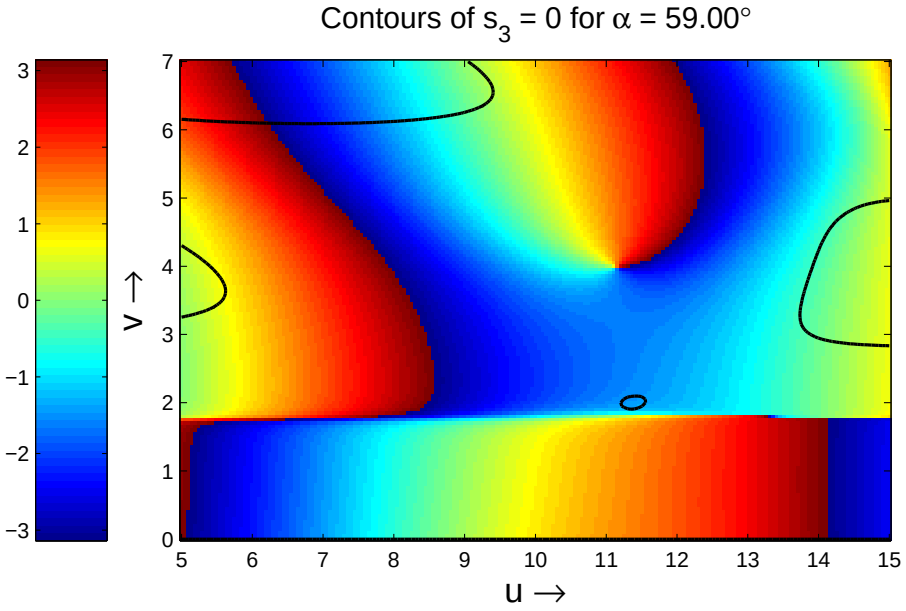

Figure B.9: A color-coded phase map of e_+ with L-lines (solid black curves) superposed and the semiaperture angle 59.00° with β kept fixed at 1.5.

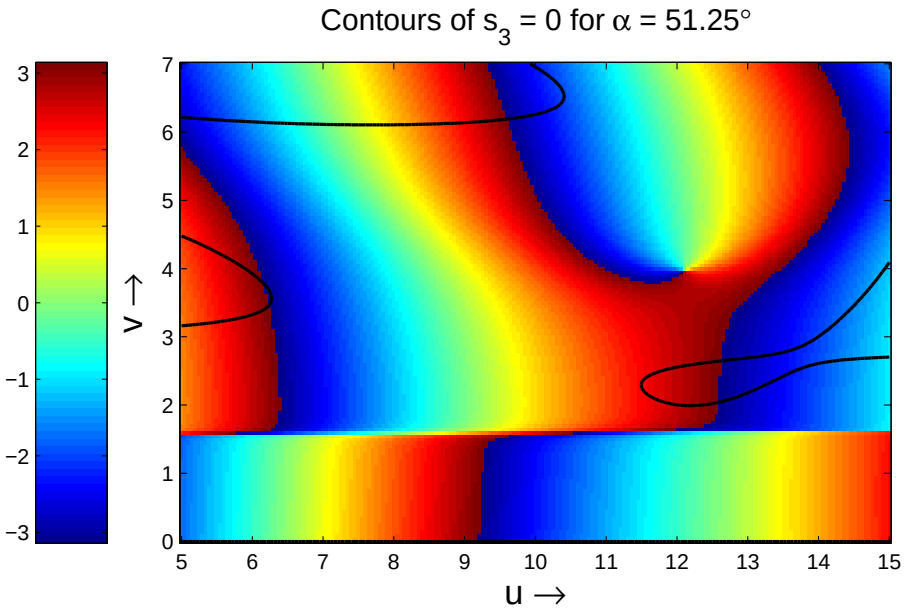

Figure B.10: A color-coded phase map of e_+ with L-lines (solid black curves) superposed and the semiaperture angle 51.25° with β kept fixed at 1.5.

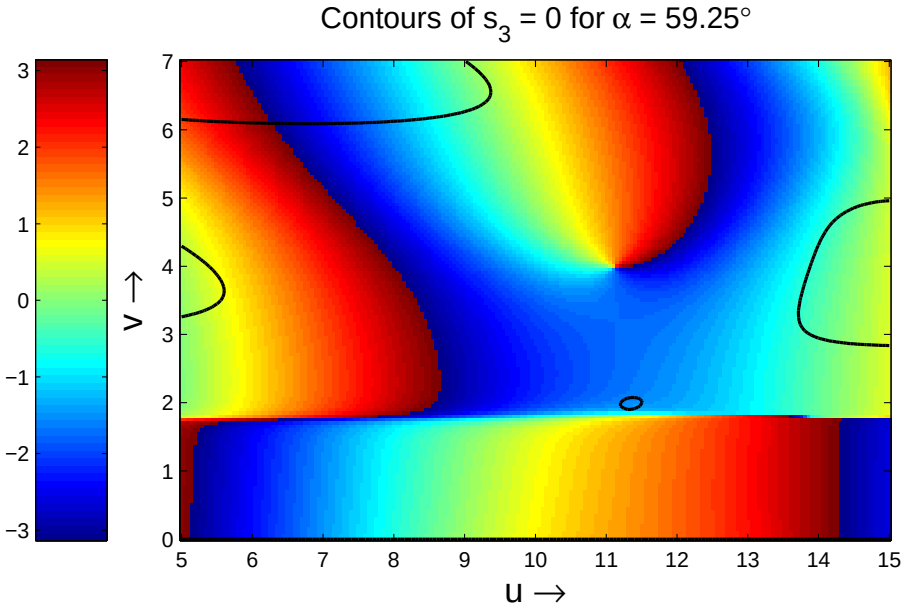

Figure B.11: A color-coded phase map of e_+ with L-lines (solid black curves) superposed and the semiaperture angle 59.25° with β kept fixed at 1.5.

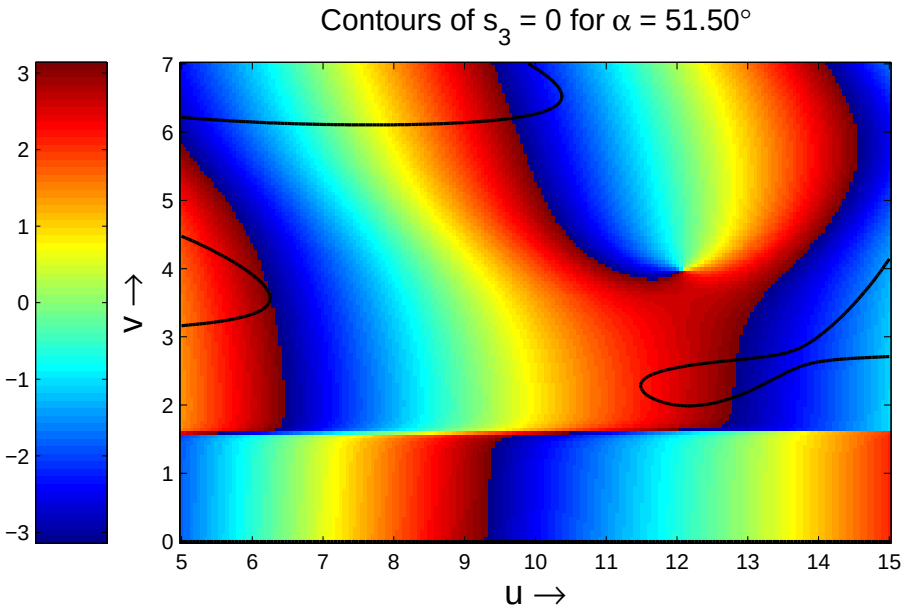

Figure B.12: A color-coded phase map of e_+ with L-lines (solid black curves) superposed and the semiaperture angle 51.50° with β kept fixed at 1.5.

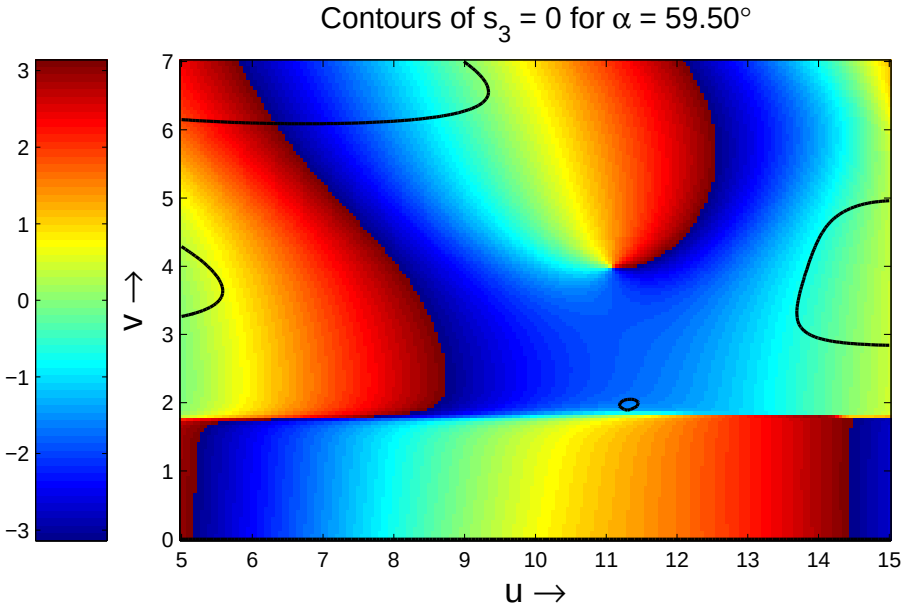

Figure B.13: A color-coded phase map of e_+ with L-lines (solid black curves) superposed and the semiaperture angle 59.50° with β kept fixed at 1.5.

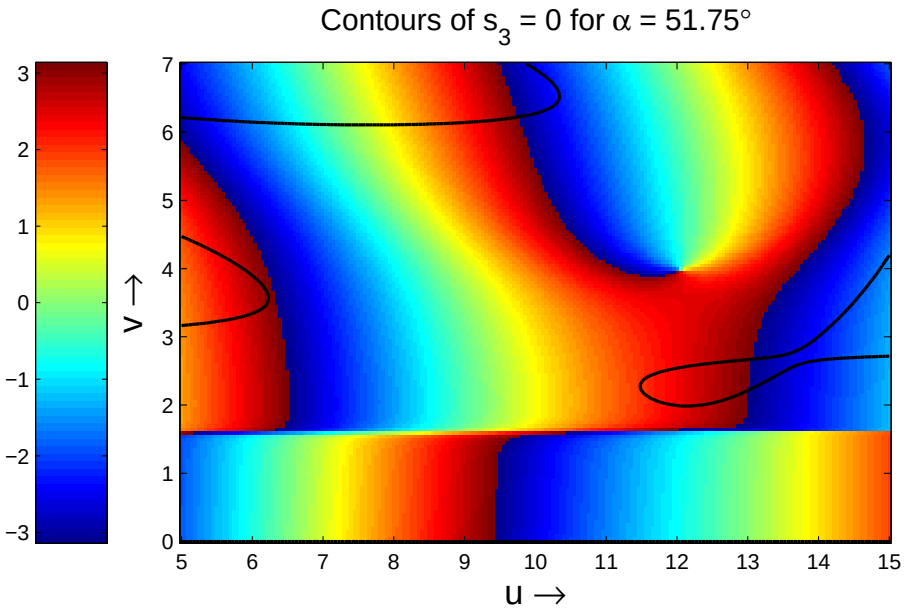

Figure B.14: A color-coded phase map of e_+ with L-lines (solid black curves) superposed and the semiaperture angle 51.75° with β kept fixed at 1.5.

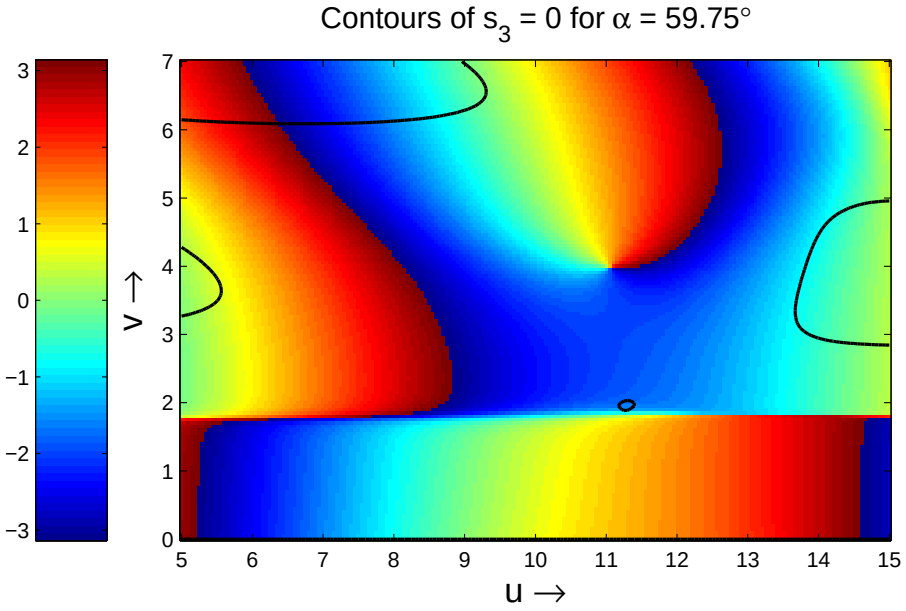

Figure B.15: A color-coded phase map of e_+ with L-lines (solid black curves) superposed and the semiaperture angle 59.75° with β kept fixed at 1.5.

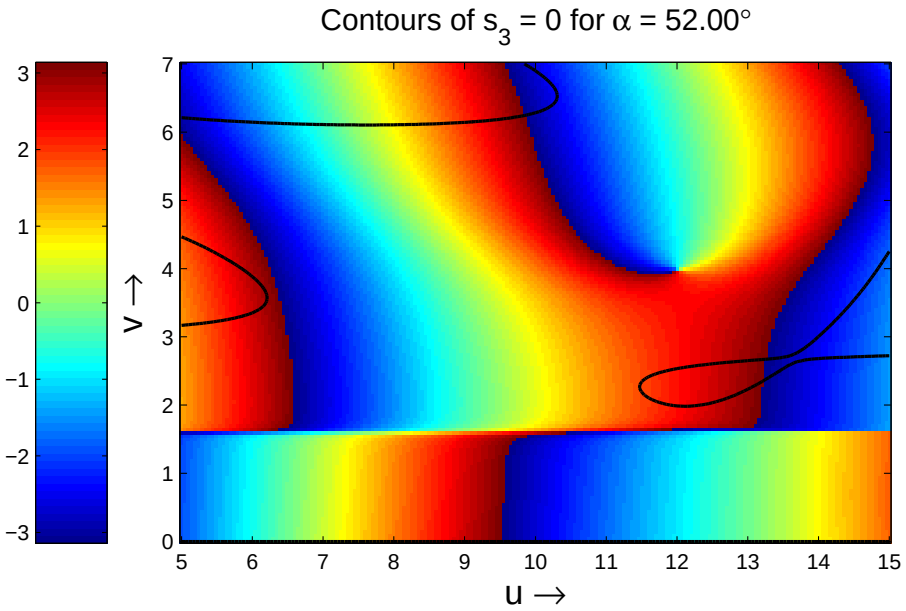

Figure B.16: A color-coded phase map of e_+ with L-lines (solid black curves) superposed and the semiaperture angle 52.00° with β kept fixed at 1.5.

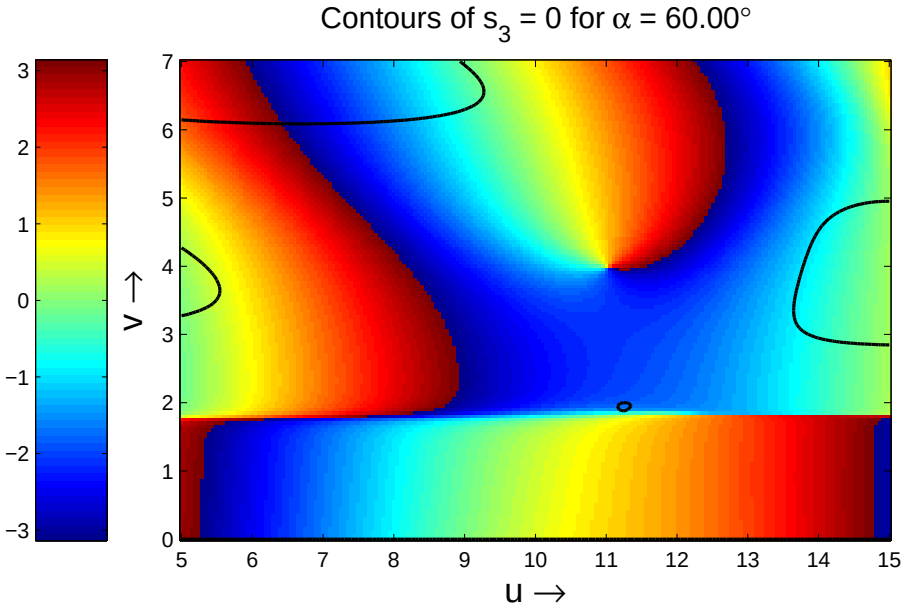

Figure B.17: A color-coded phase map of e_+ with L-lines (solid black curves) superposed and the semiaperture angle 60.00° with β kept fixed at 1.5.

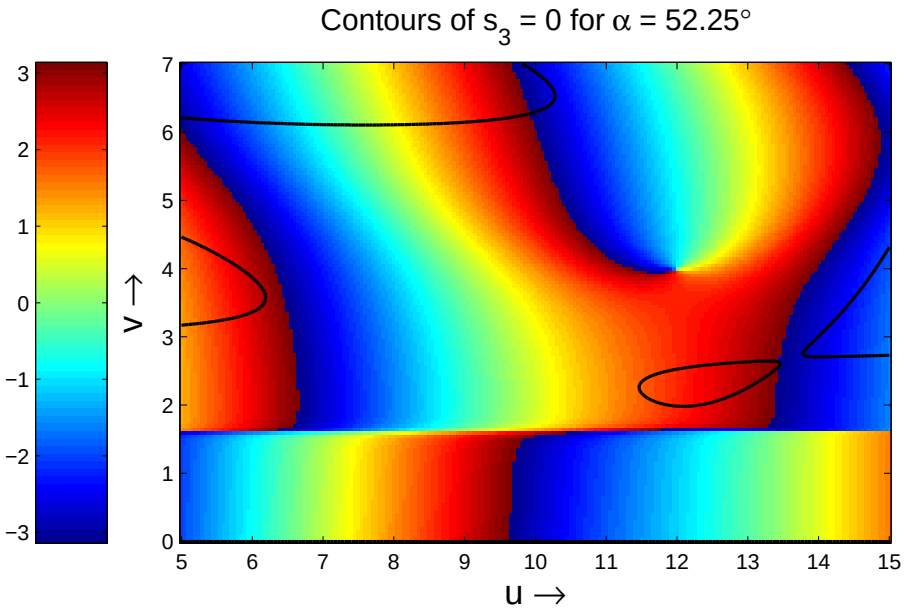

Figure B.18: A color-coded phase map of e_+ with L-lines (solid black curves) superposed and the semiaperture angle 52.25° with β kept fixed at 1.5.

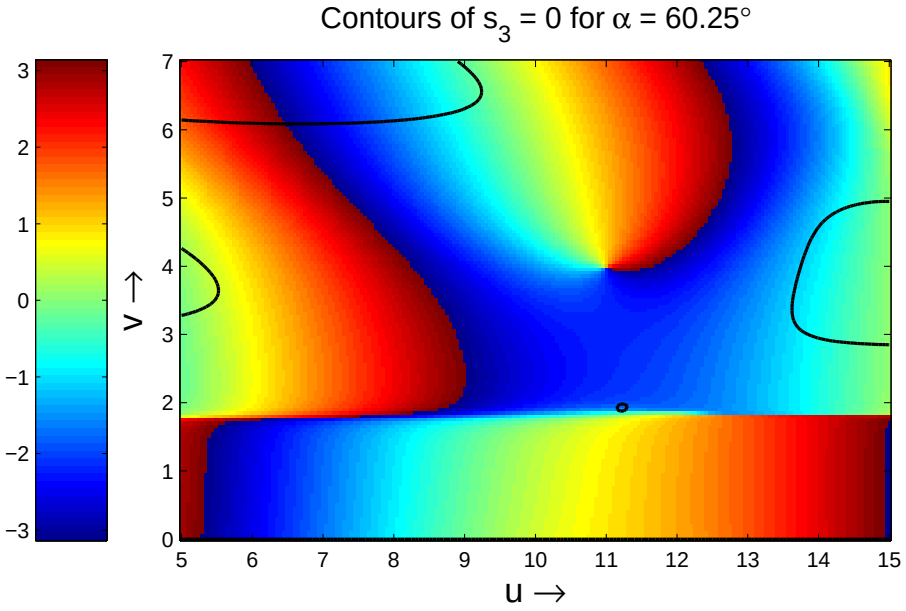

Figure B.19: A color-coded phase map of e_+ with L-lines (solid black curves) superposed and the semiaperture angle 60.25° with β kept fixed at 1.5.

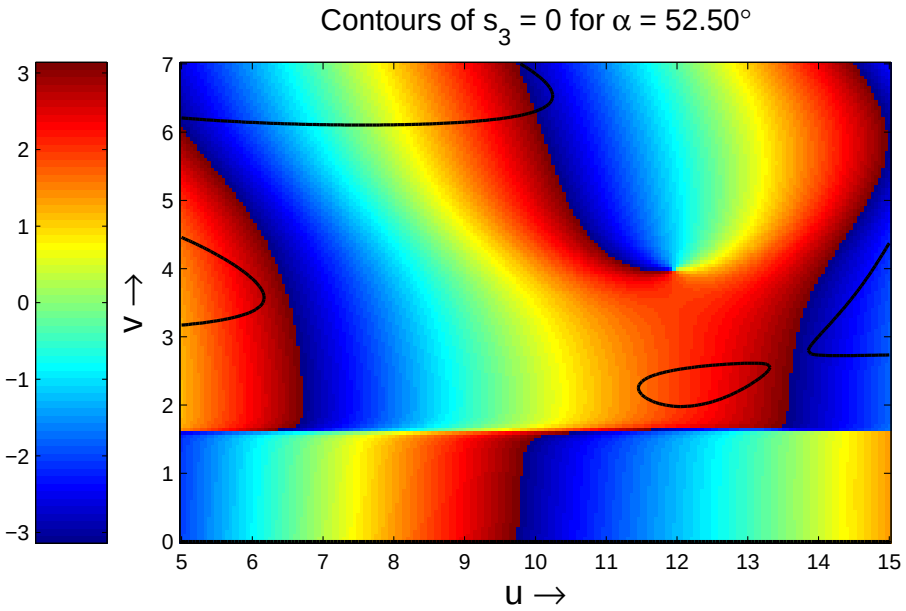

Figure B.20: A color-coded phase map of e_+ with L-lines (solid black curves) superposed and the semiaperture angle 52.50° with β kept fixed at 1.5.

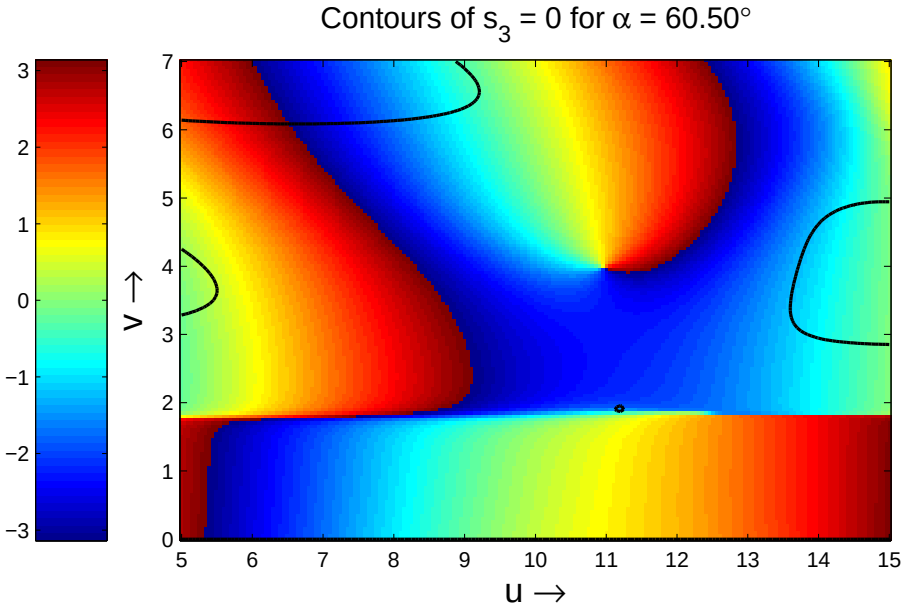

Figure B.21: A color-coded phase map of e_+ with L-lines (solid black curves) superposed and the semiaperture angle 60.50° with β kept fixed at 1.5.

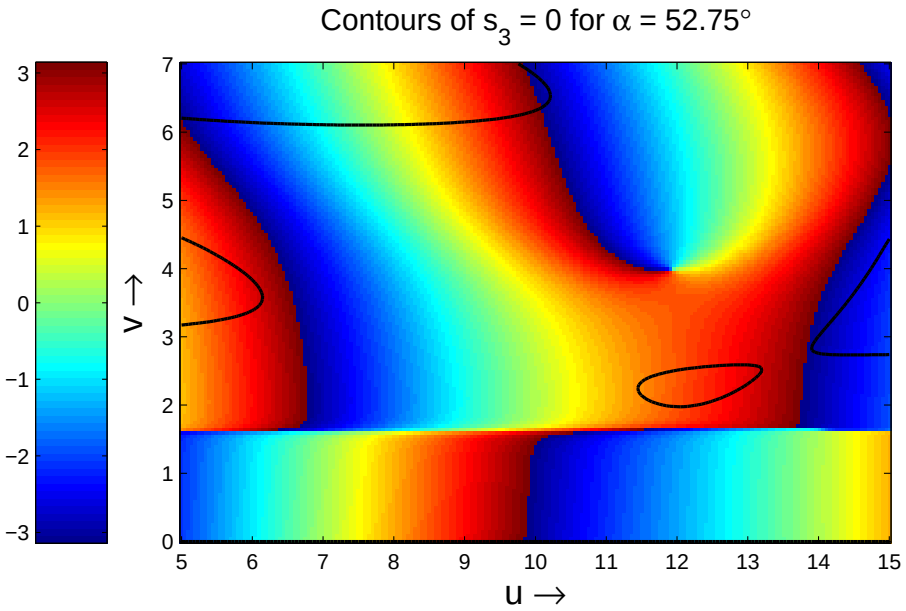

Figure B.22: A color-coded phase map of e_+ with L-lines (solid black curves) superposed and the semiaperture angle 52.75° with β kept fixed at 1.5.

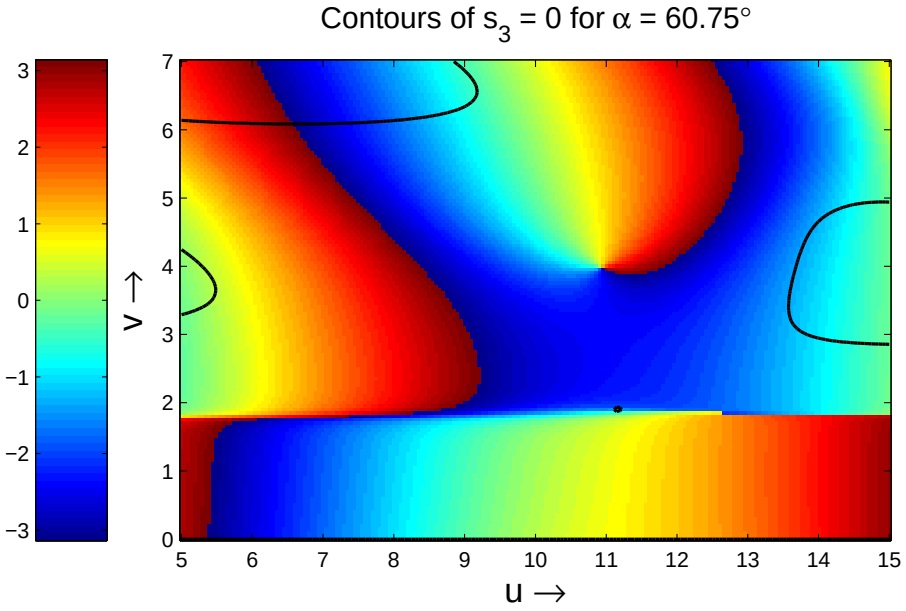

Figure B.23: A color-coded phase map of e_+ with L-lines (solid black curves) superposed and the semiaperture angle 60.75° with β kept fixed at 1.5.

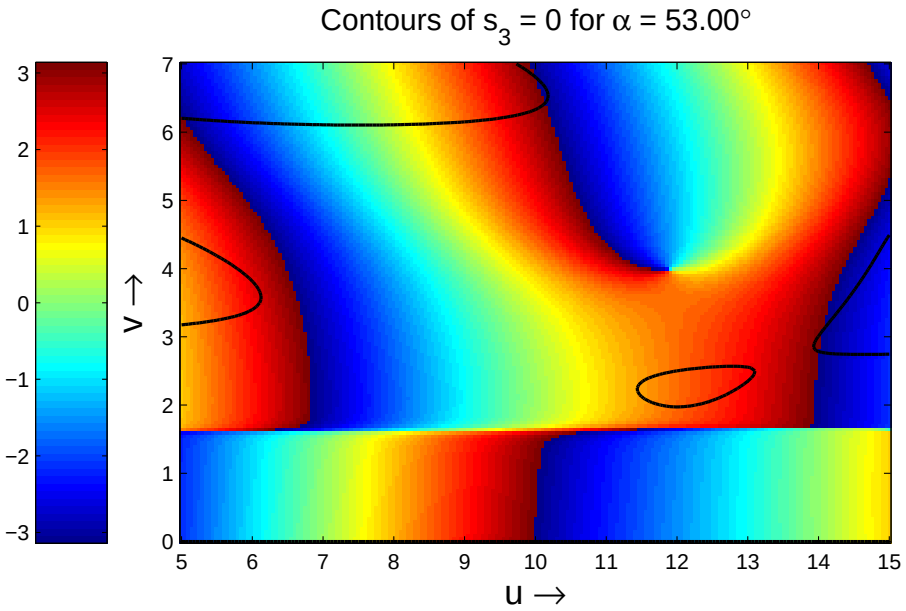

Figure B.24: A color-coded phase map of e_+ with L-lines (solid black curves) superposed and the semiaperture angle 53.00° with β kept fixed at 1.5.

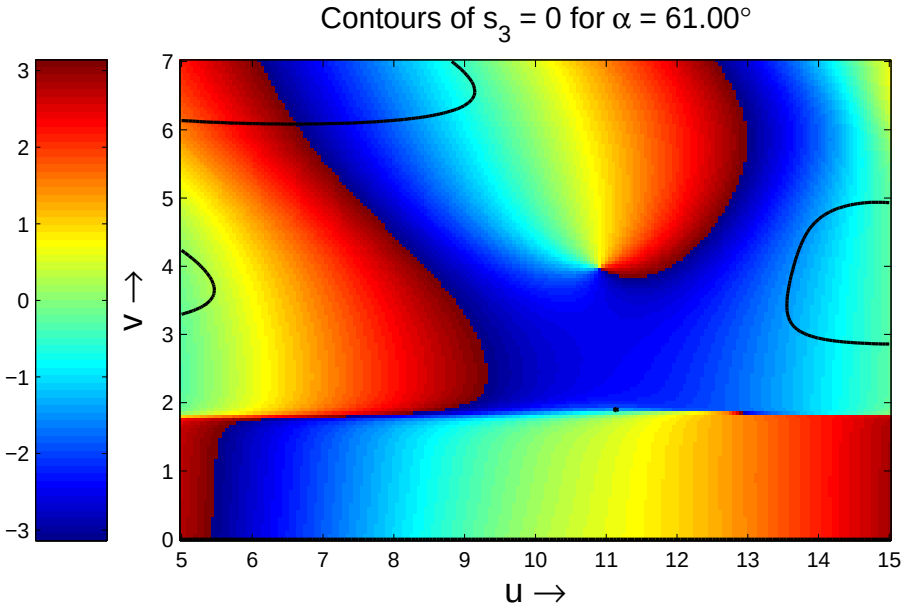

Figure B.25: A color-coded phase map of e_+ with L-lines (solid black curves) superposed and the semiaperture angle 61.00° with β kept fixed at 1.5.

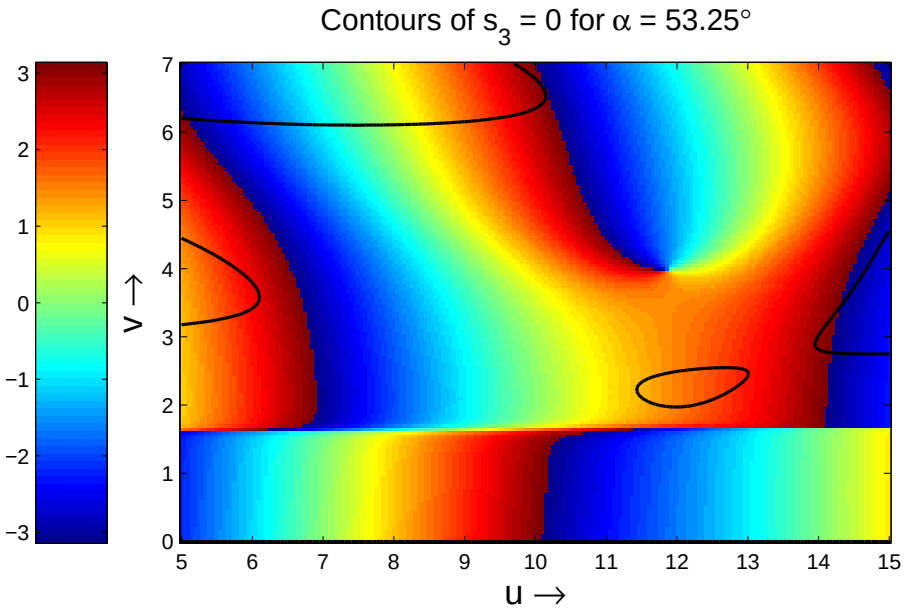

Figure B.26: A color-coded phase map of e_+ with L-lines (solid black curves) superposed and the semiaperture angle 53.25° with β kept fixed at 1.5.

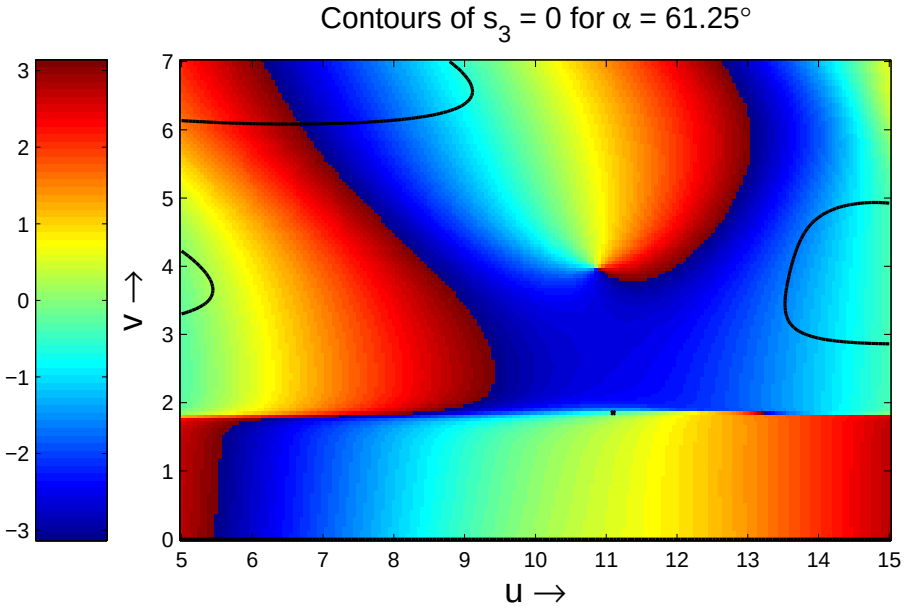

Figure B.27: A color-coded phase map of e_+ with L-lines (solid black curves) superposed and the semiaperture angle 61.25° with β kept fixed at 1.5.

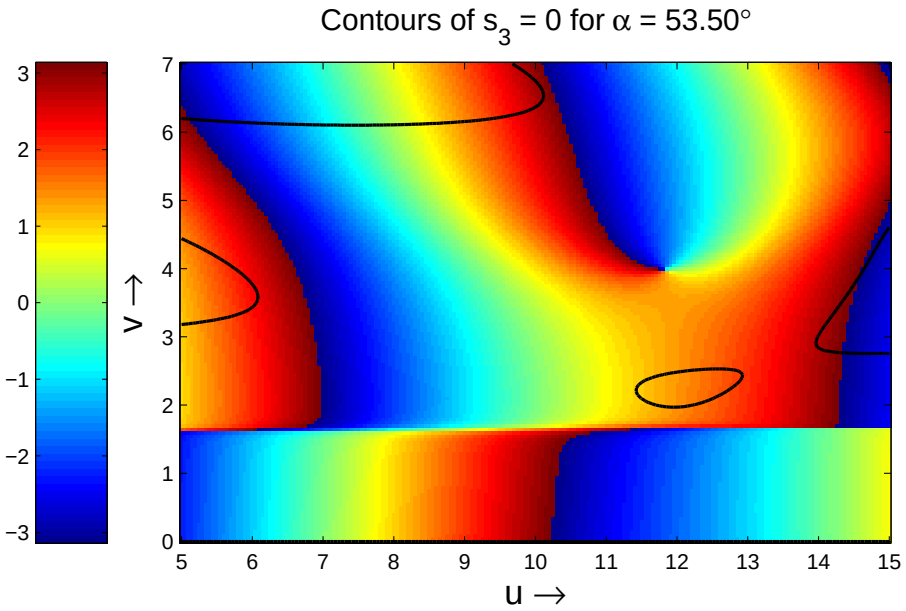

Figure B.28: A color-coded phase map of e_+ with L-lines (solid black curves) superposed and the semiaperture angle 53.50° with β kept fixed at 1.5.

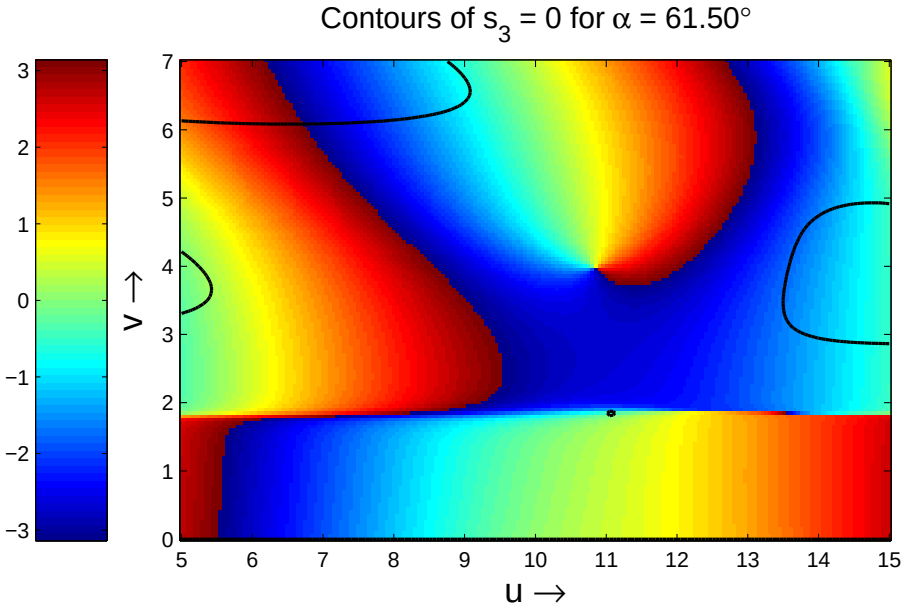

Figure B.29: A color-coded phase map of e_+ with L-lines (solid black curves) superposed and the semiaperture angle 61.50° with β kept fixed at 1.5.

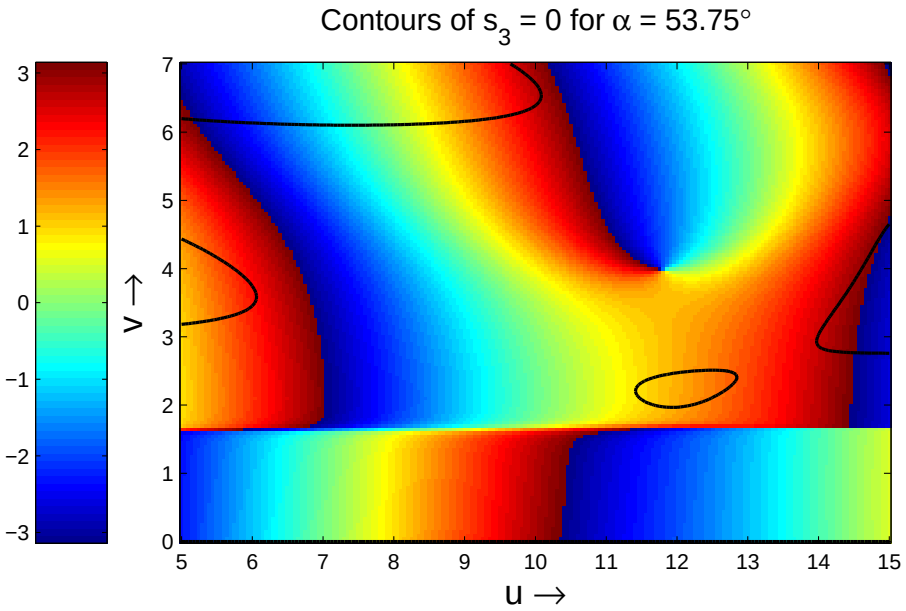

Figure B.30: A color-coded phase map of e_+ with L-lines (solid black curves) superposed and the semiaperture angle 53.75° with β kept fixed at 1.5.

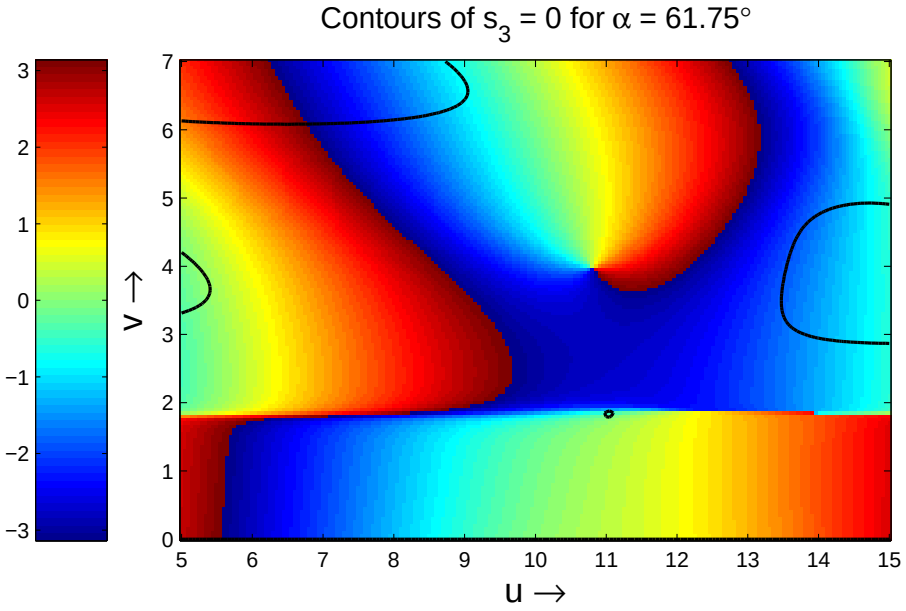

Figure B.31: A color-coded phase map of e_+ with L-lines (solid black curves) superposed and the semiaperture angle 61.75° with β kept fixed at 1.5.

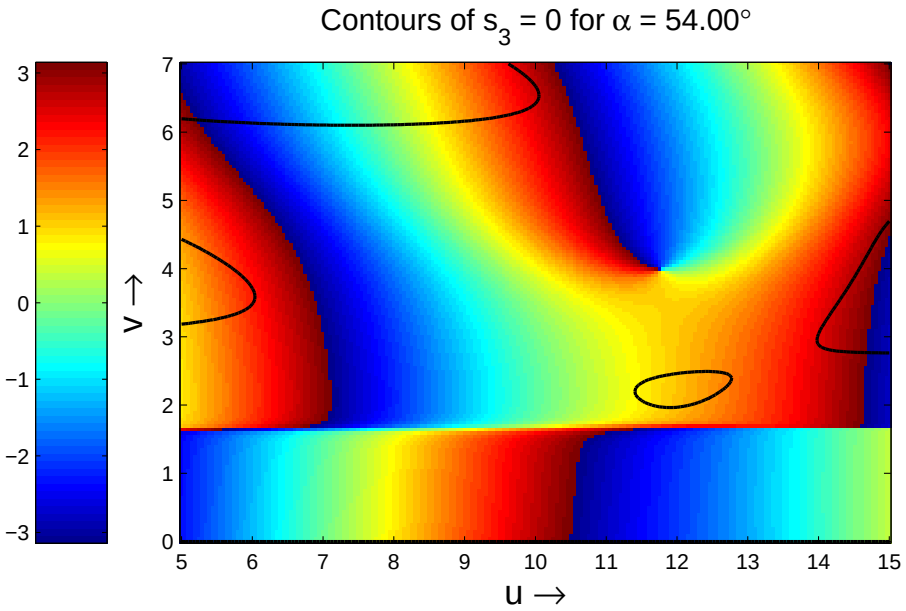

Figure B.32: A color-coded phase map of e_+ with L-lines (solid black curves) superposed and the semiaperture angle 54.00° with β kept fixed at 1.5.

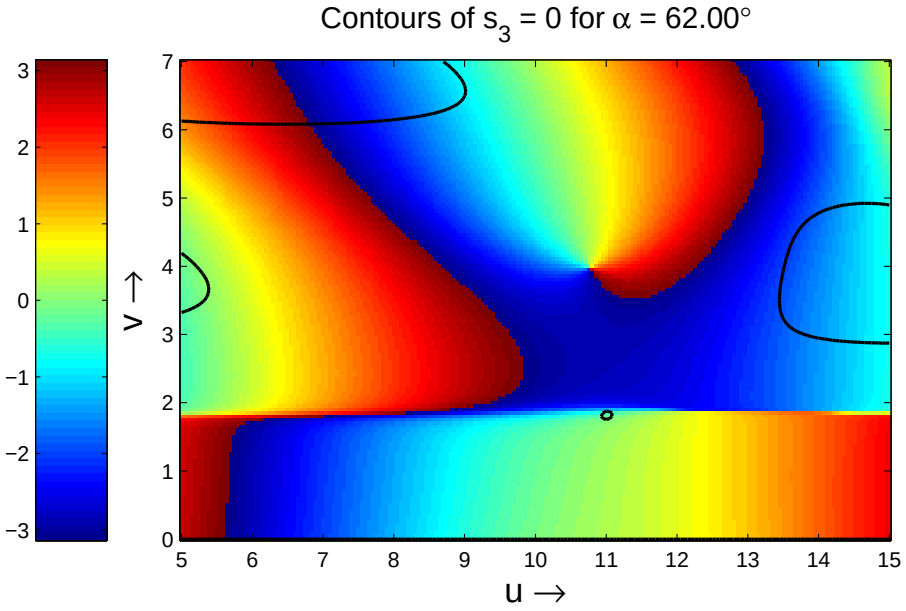

Figure B.33: A color-coded phase map of e_+ with L-lines (solid black curves) superposed and the semiaperture angle 62.00° with β kept fixed at 1.5.

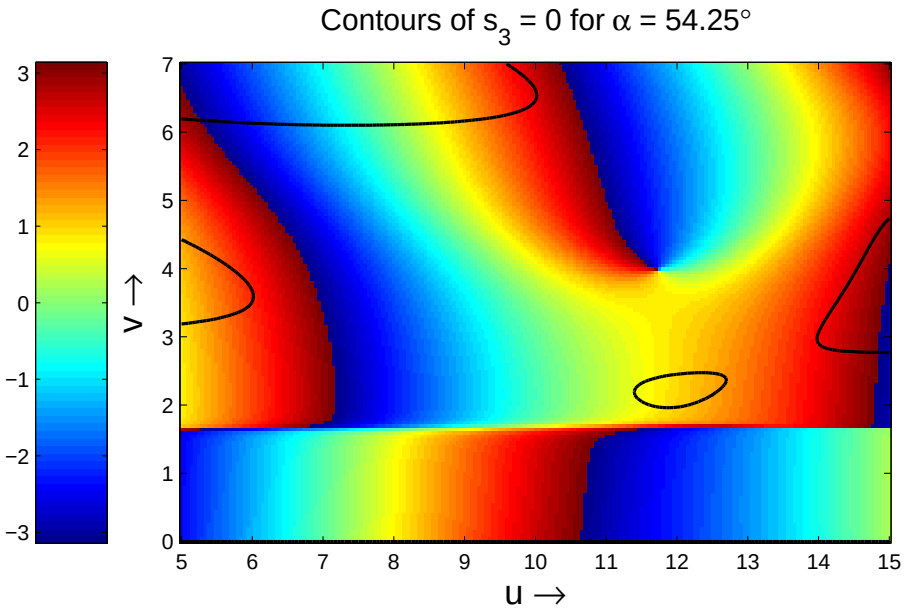

Figure B.34: A color-coded phase map of e_+ with L-lines (solid black curves) superposed and the semiaperture angle 54.25° with β kept fixed at 1.5.

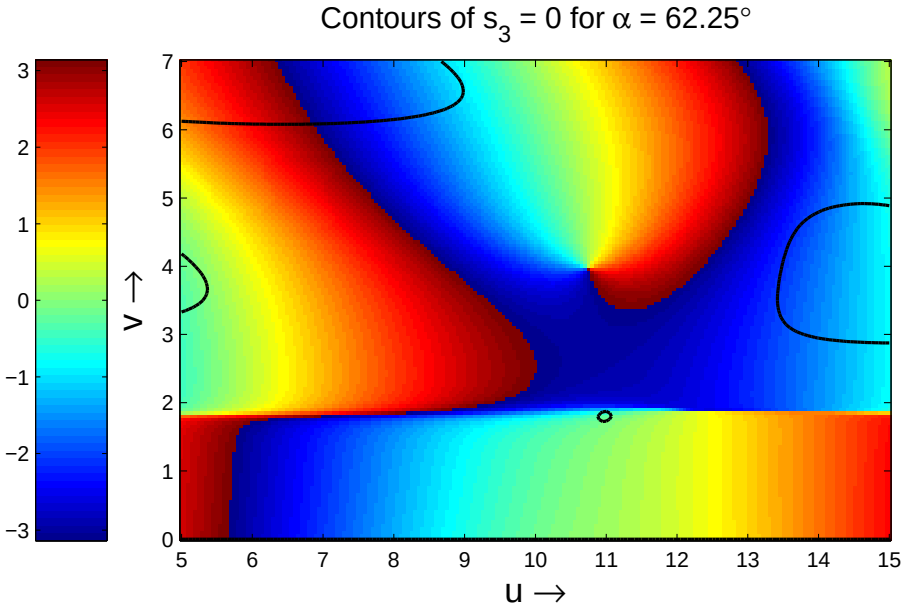

Figure B.35: A color-coded phase map of e_+ with L-lines (solid black curves) superposed and the semiaperture angle 62.25° with β kept fixed at 1.5.

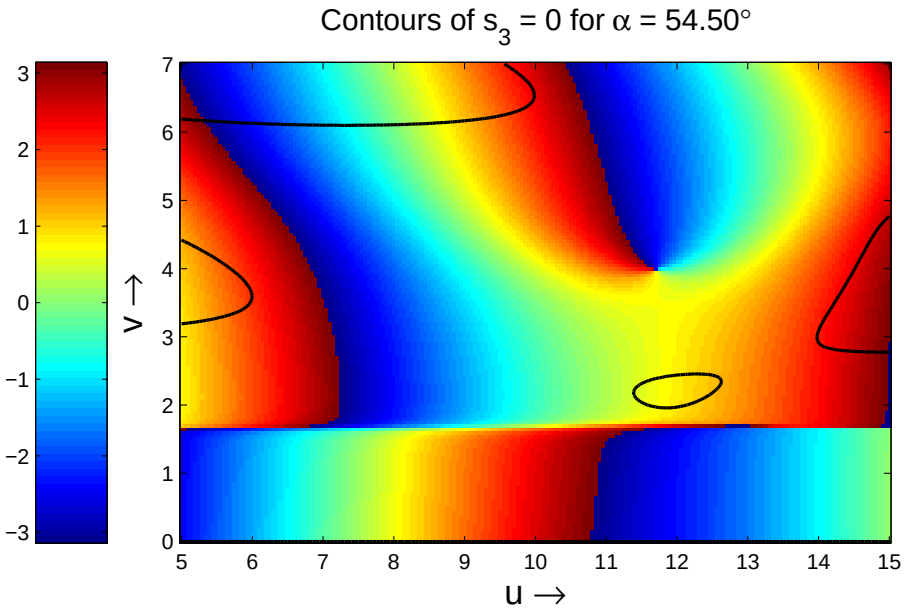

Figure B.36: A color-coded phase map of e_+ with L-lines (solid black curves) superposed and the semiaperture angle 54.50° with β kept fixed at 1.5.

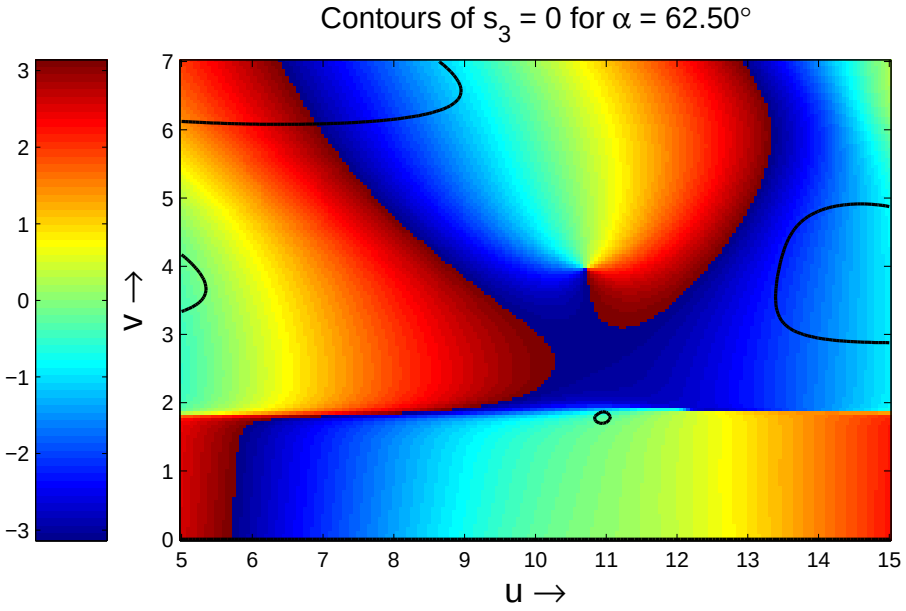

Figure B.37: A color-coded phase map of e_+ with L-lines (solid black curves) superposed and the semiaperture angle 62.50° with β kept fixed at 1.5.

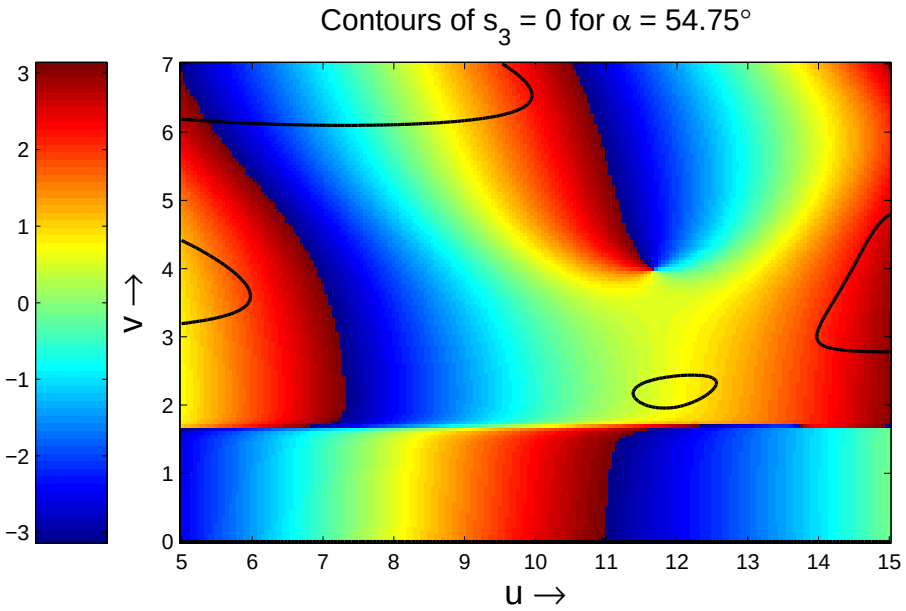

Figure B.38: A color-coded phase map of e_+ with L-lines (solid black curves) superposed and the semiaperture angle 54.75° with β kept fixed at 1.5.

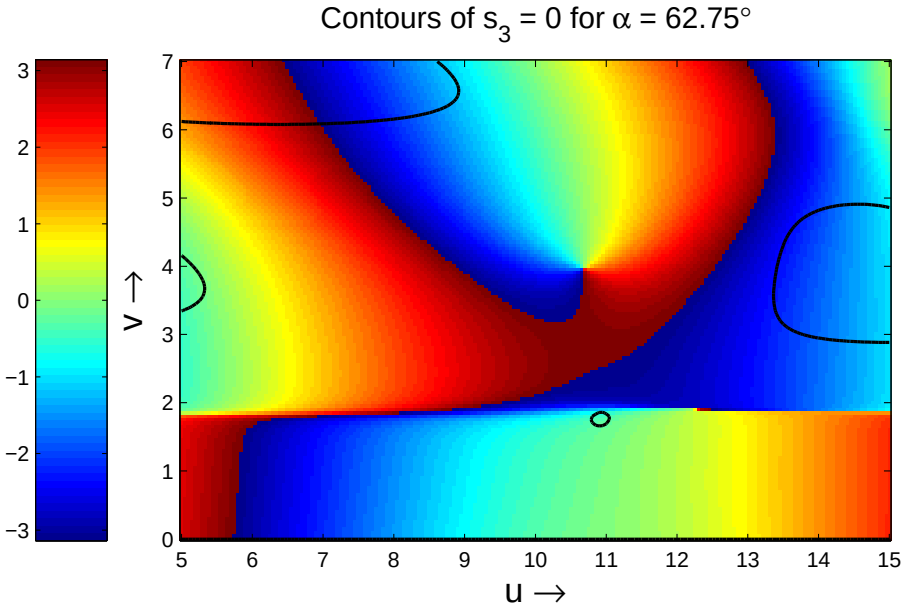

Figure B.39: A color-coded phase map of e_+ with L-lines (solid black curves) superposed and the semiaperture angle 62.75° with β kept fixed at 1.5.

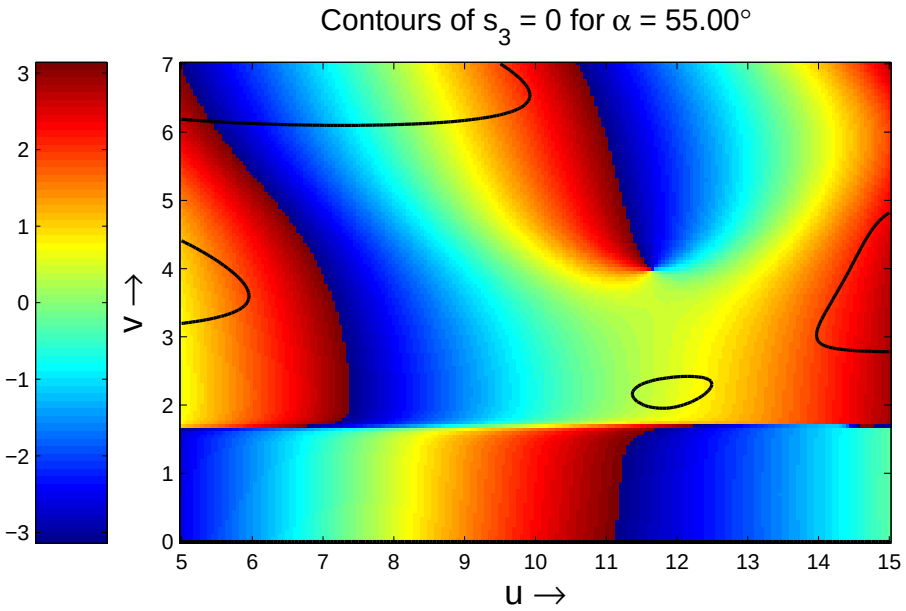

Figure B.40: A color-coded phase map of e_+ with L-lines (solid black curves) superposed and the semiaperture angle 55.00° with β kept fixed at 1.5.

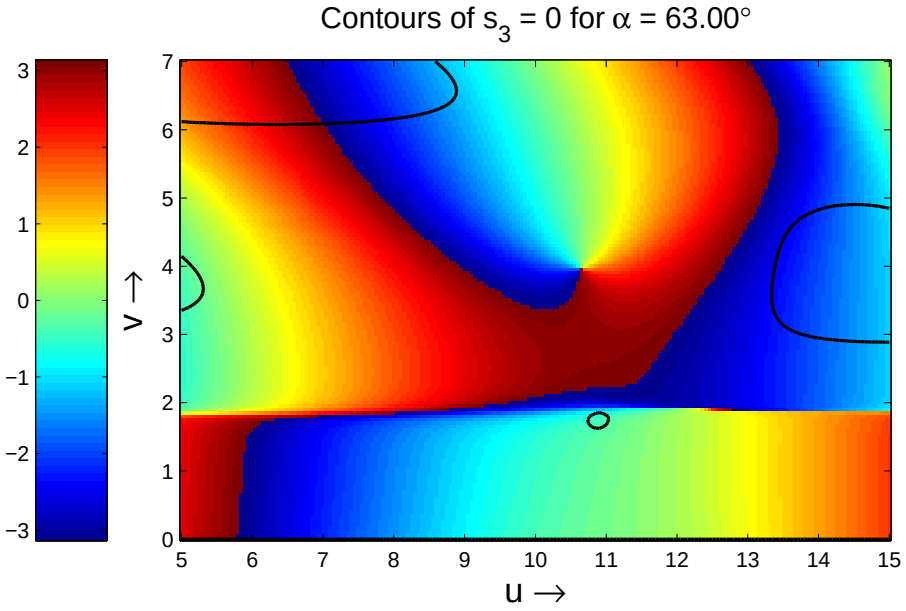

Figure B.41: A color-coded phase map of e_+ with L-lines (solid black curves) superposed and the semiaperture angle 63.00° with β kept fixed at 1.5.

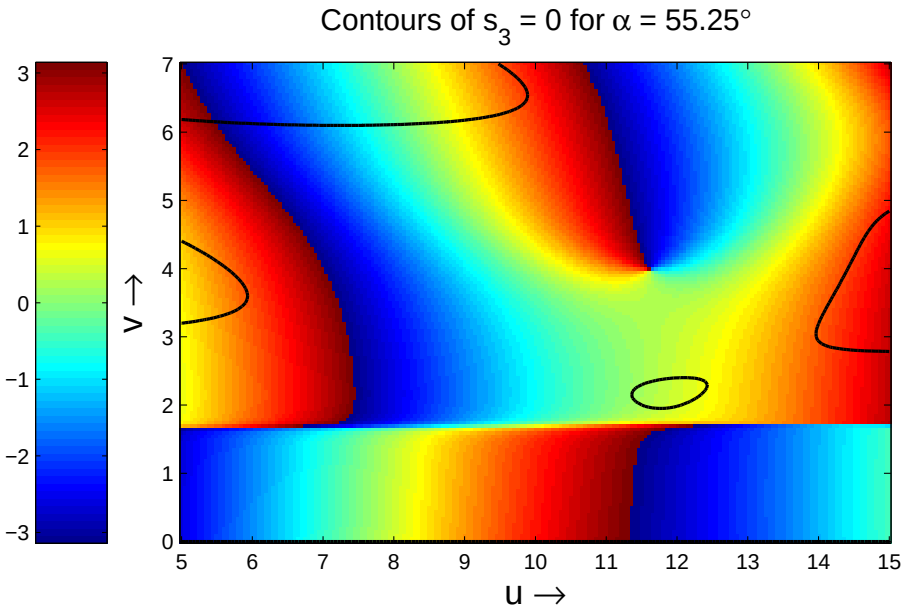

Figure B.42: A color-coded phase map of e_+ with L-lines (solid black curves) superposed and the semiaperture angle 55.25° with β kept fixed at 1.5.

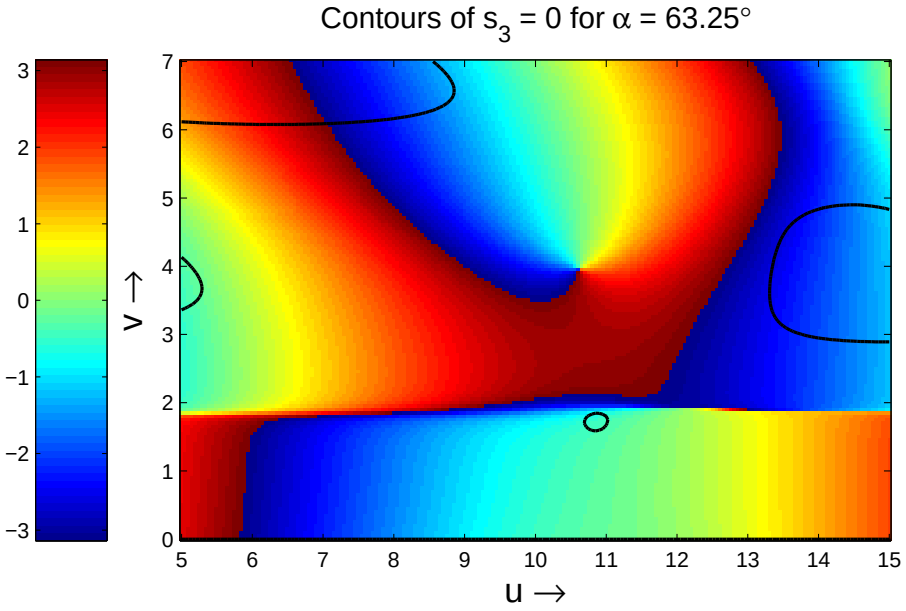

Figure B.43: A color-coded phase map of e_+ with L-lines (solid black curves) superposed and the semiaperture angle 63.25° with β kept fixed at 1.5.

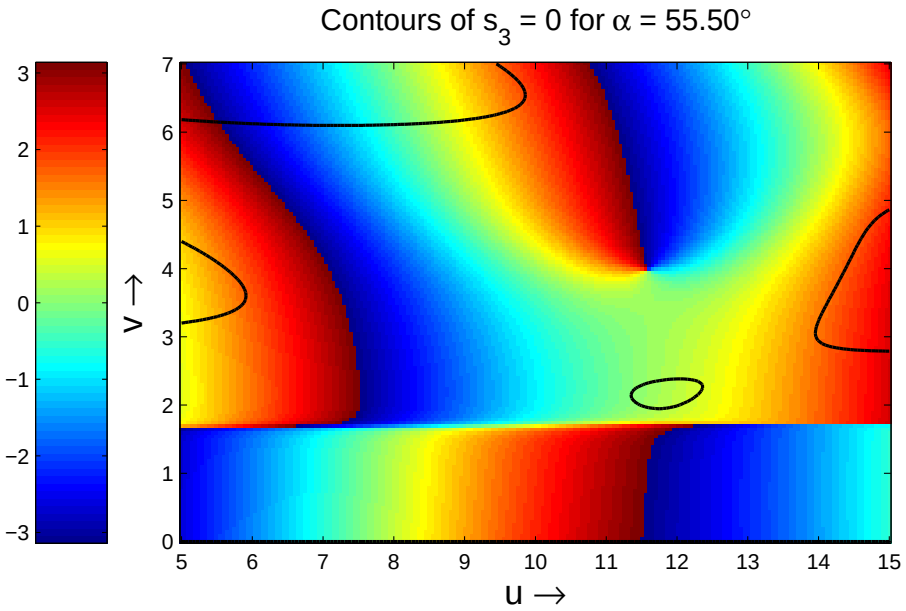

Figure B.44: A color-coded phase map of e_+ with L-lines (solid black curves) superposed and the semiaperture angle 55.50° with β kept fixed at 1.5.

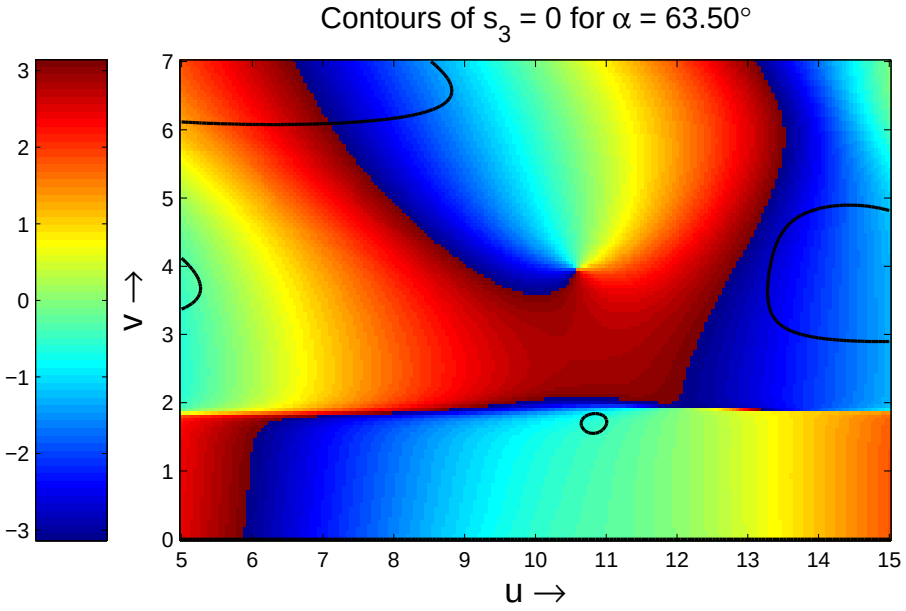

Figure B.45: A color-coded phase map of e_+ with L-lines (solid black curves) superposed and the semiaperture angle 63.50° with β kept fixed at 1.5.

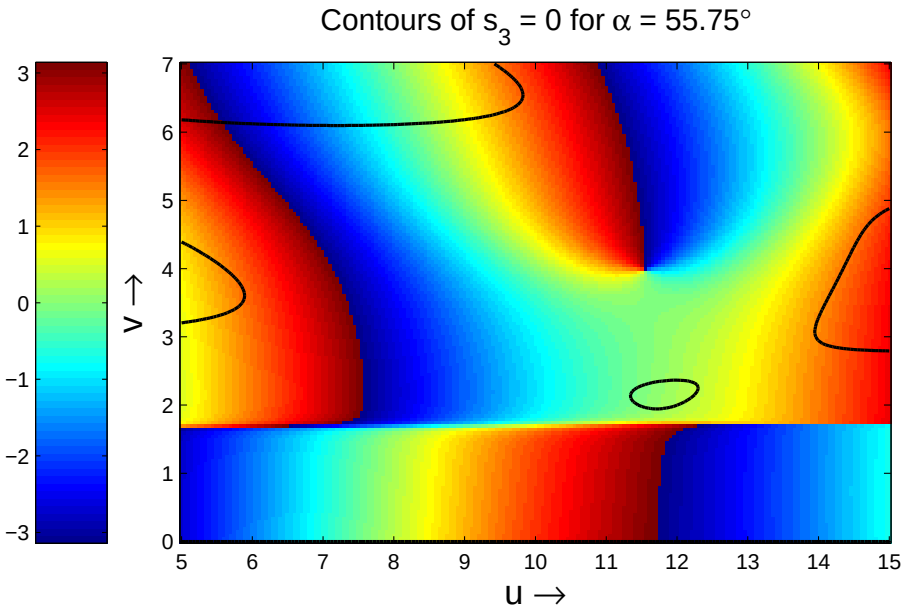

Figure B.46: A color-coded phase map of e_+ with L-lines (solid black curves) superposed and the semiaperture angle 55.75° with β kept fixed at 1.5.

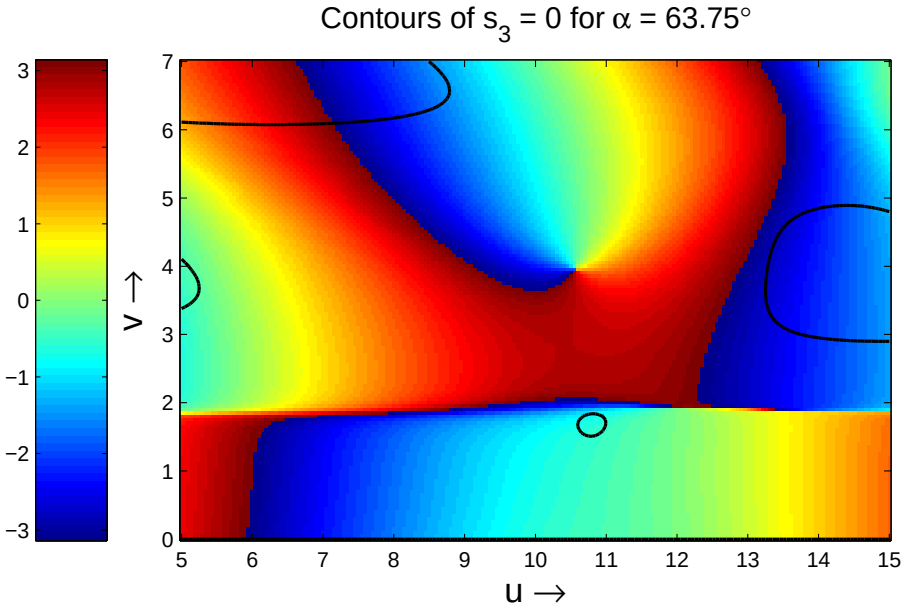

Figure B.47: A color-coded phase map of e_+ with L-lines (solid black curves) superposed and the semiaperture angle 63.75° with β kept fixed at 1.5.

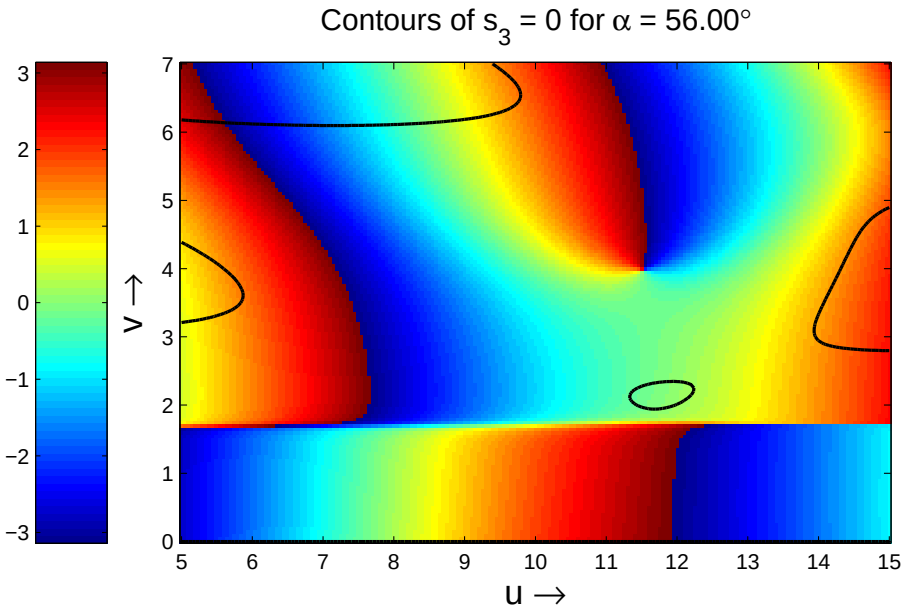

Figure B.48: A color-coded phase map of e_+ with L-lines (solid black curves) superposed and the semiaperture angle 56.00° with β kept fixed at 1.5.

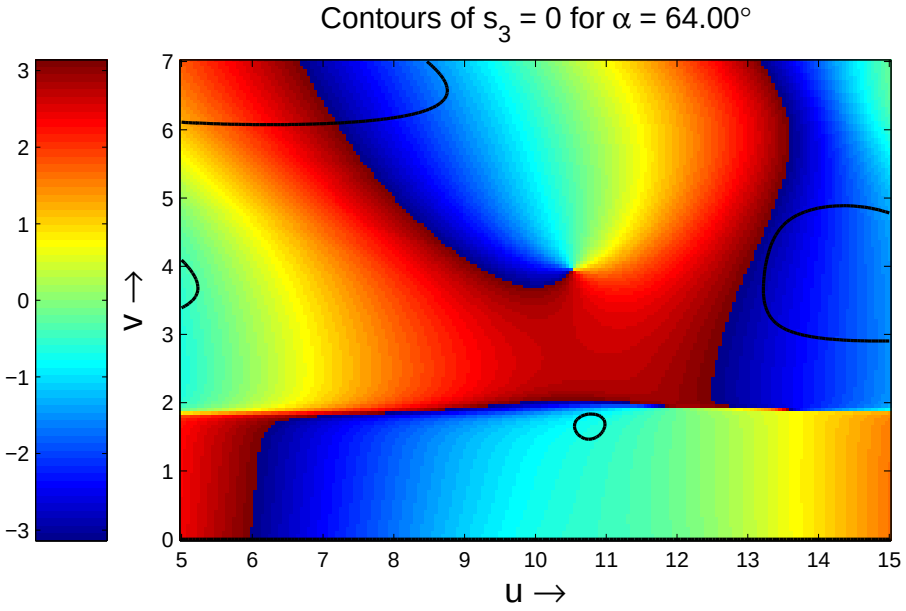

Figure B.49: A color-coded phase map of e_+ with L-lines (solid black curves) superposed and the semiaperture angle 64.00° with β kept fixed at 1.5.

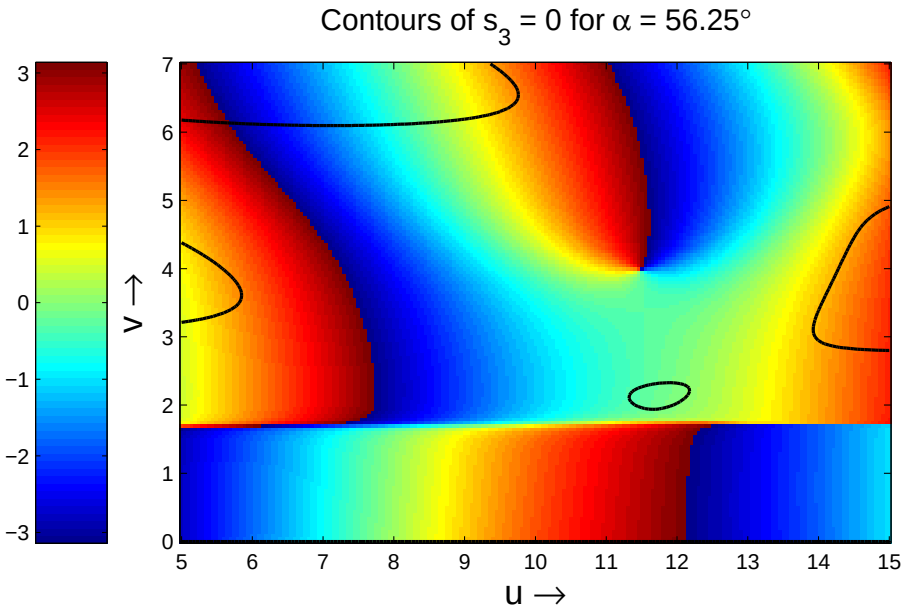

Figure B.50: A color-coded phase map of e_+ with L-lines (solid black curves) superposed and the semiaperture angle 56.25° with β kept fixed at 1.5.

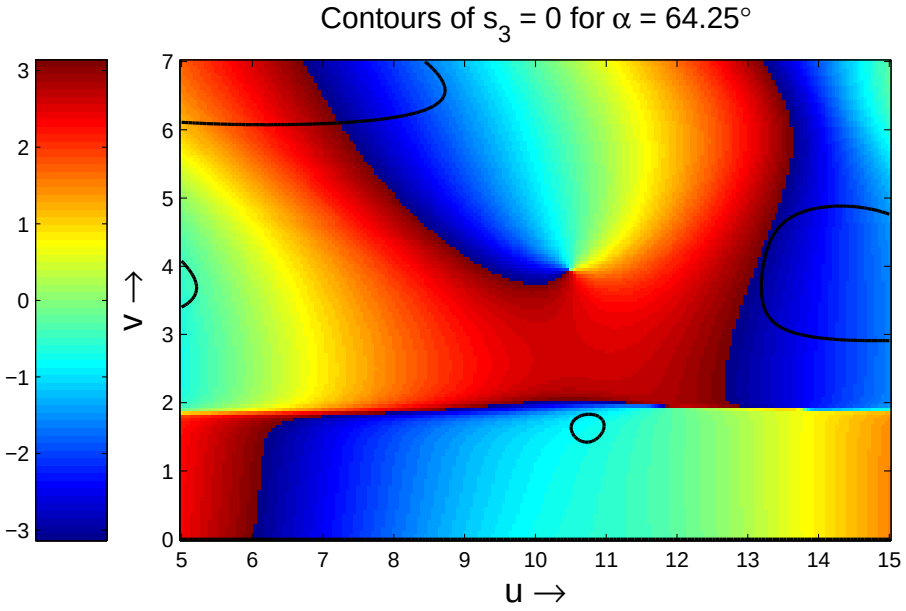

Figure B.51: A color-coded phase map of e_+ with L-lines (solid black curves) superposed and the semiaperture angle 64.25° with β kept fixed at 1.5.

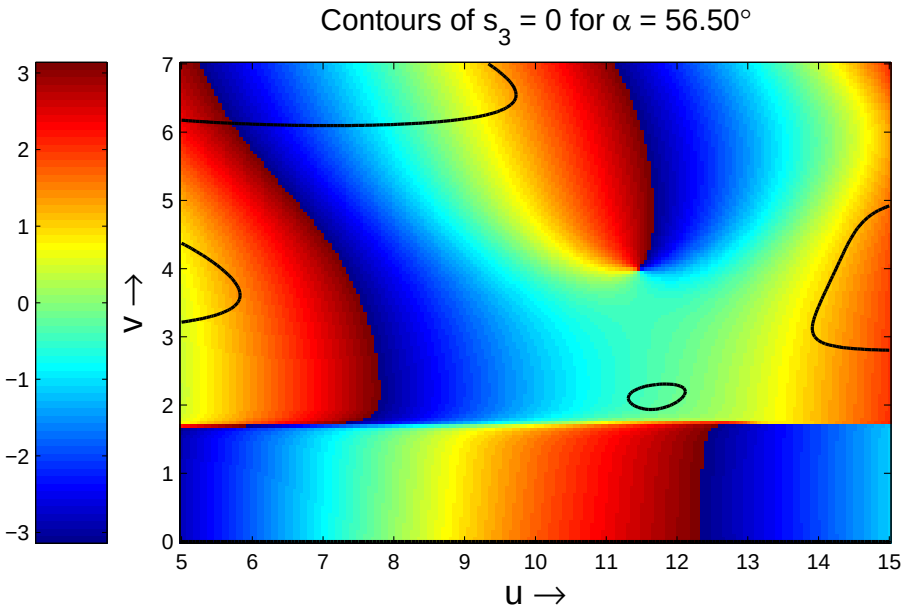

Figure B.52: A color-coded phase map of e_+ with L-lines (solid black curves) superposed and the semiaperture angle 56.50° with β kept fixed at 1.5.

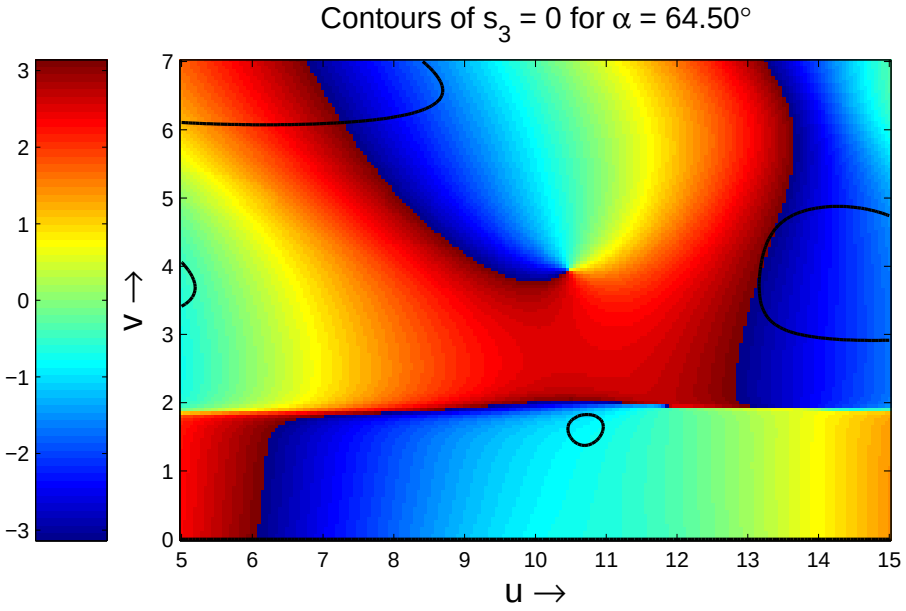

Figure B.53: A color-coded phase map of e_+ with L-lines (solid black curves) superposed and the semiaperture angle 64.50° with β kept fixed at 1.5.

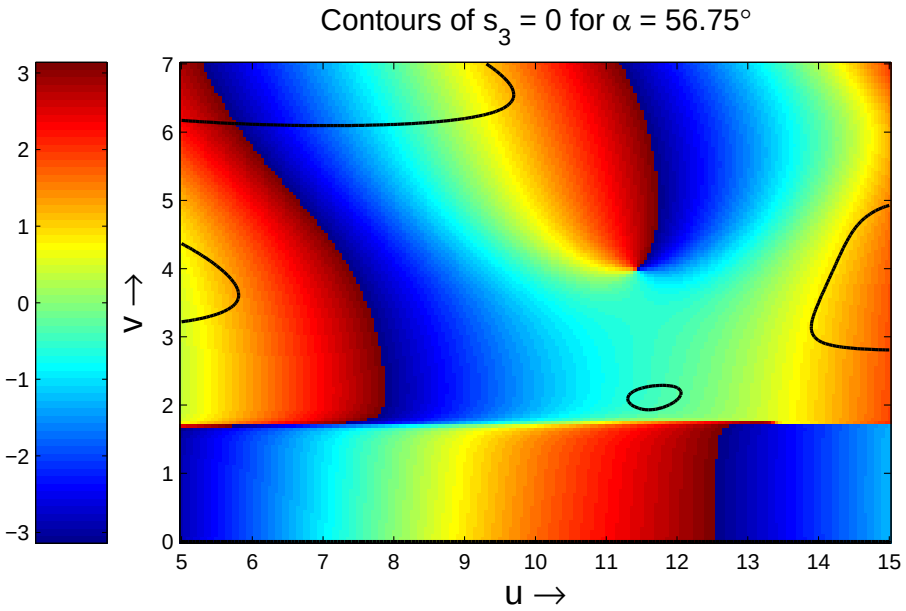

Figure B.54: A color-coded phase map of e_+ with L-lines (solid black curves) superposed and the semiaperture angle 56.75° with β kept fixed at 1.5.

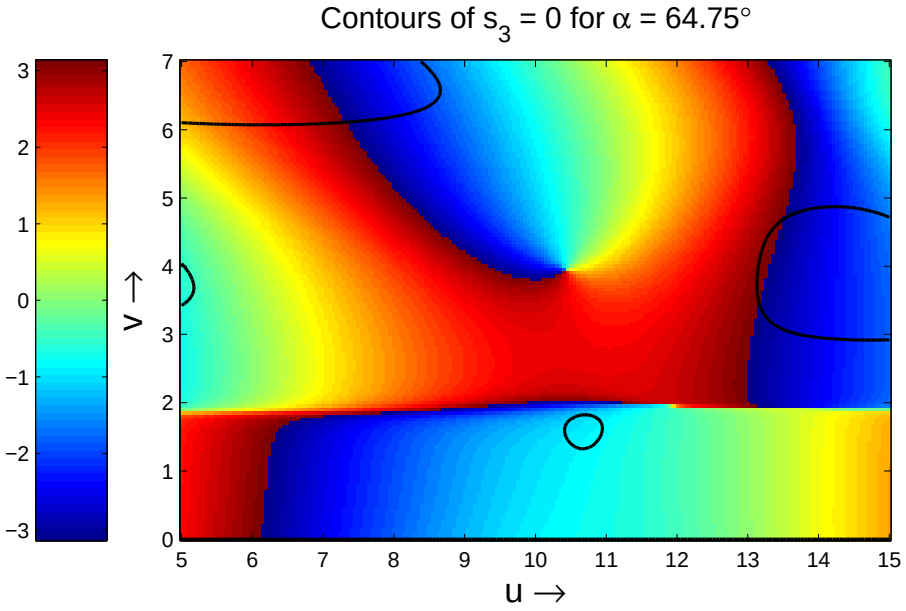

Figure B.55: A color-coded phase map of e_+ with L-lines (solid black curves) superposed and the semiaperture angle 64.75° with β kept fixed at 1.5.

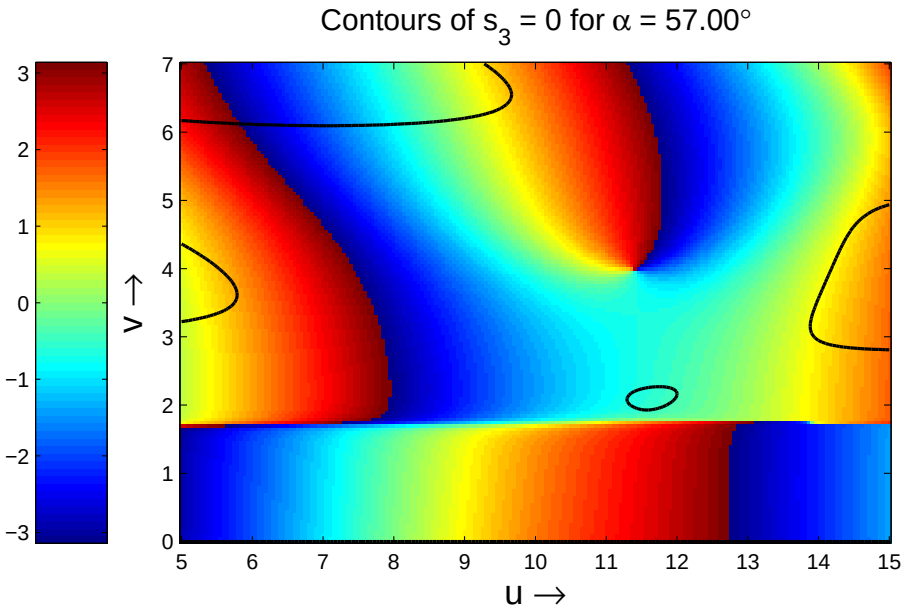

Figure B.56: A color-coded phase map of e_+ with L-lines (solid black curves) superposed and the semiaperture angle 57.00° with β kept fixed at 1.5.

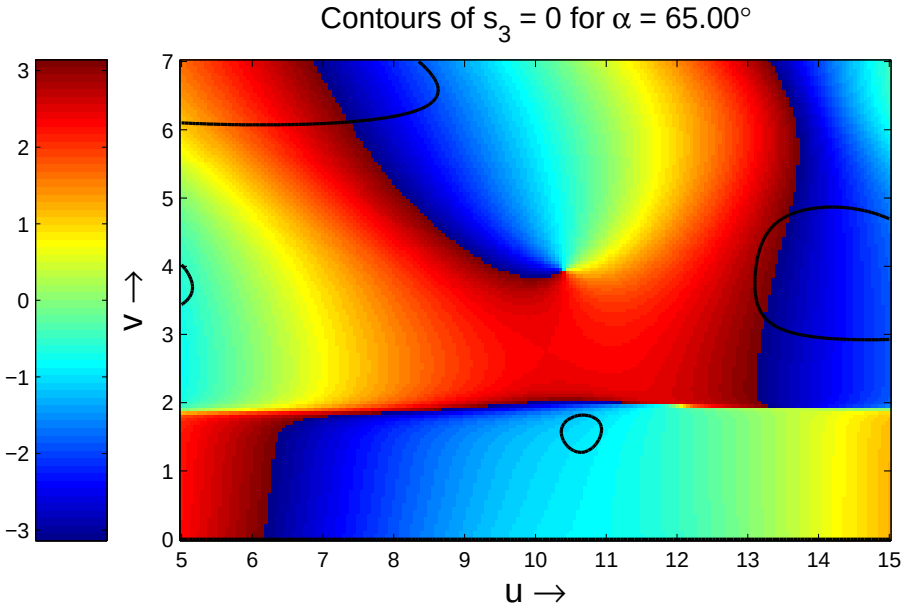

Figure B.57: A color-coded phase map of e_+ with L-lines (solid black curves) superposed and the semiaperture angle 65.00° with β kept fixed at 1.5.

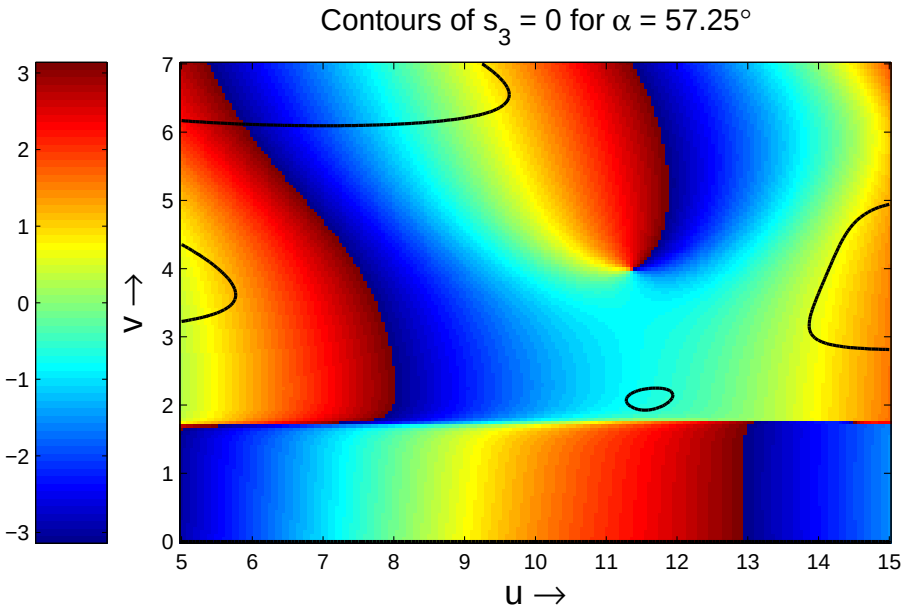

Figure B.58: A color-coded phase map of e_+ with L-lines (solid black curves) superposed and the semiaperture angle 57.25° with β kept fixed at 1.5.

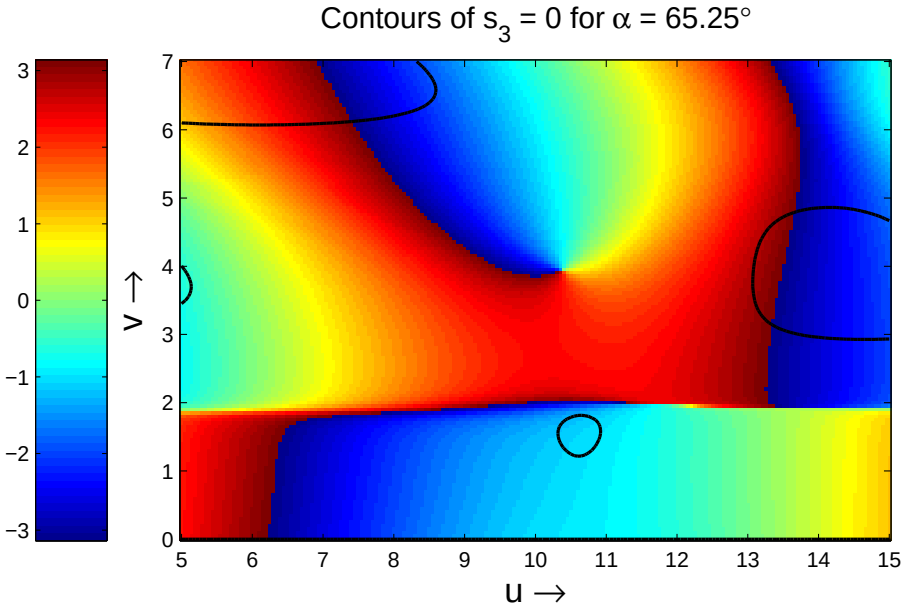

Figure B.59: A color-coded phase map of e_+ with L-lines (solid black curves) superposed and the semiaperture angle 65.25° with β kept fixed at 1.5.

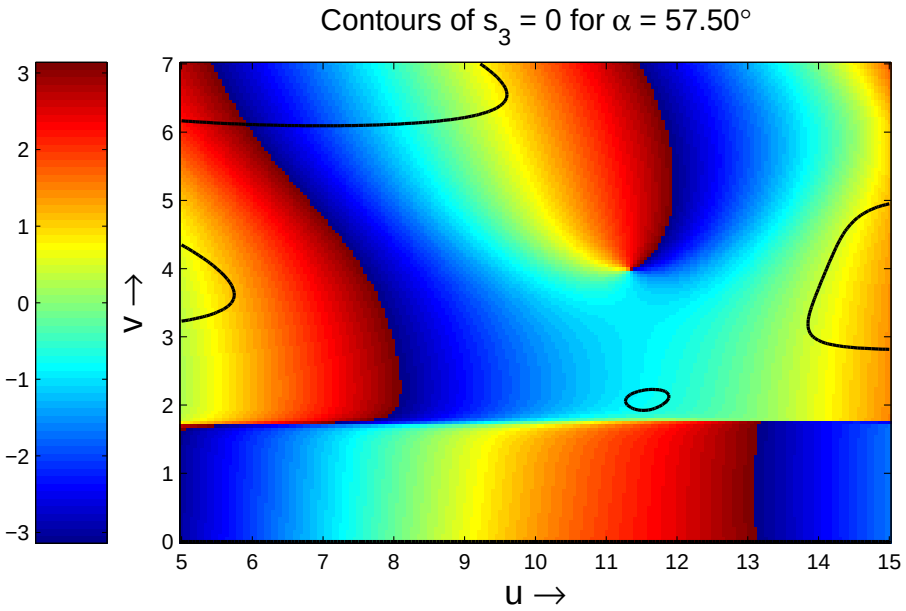

Figure B.60: A color-coded phase map of e_+ with L-lines (solid black curves) superposed and the semiaperture angle 57.50° with β kept fixed at 1.5.

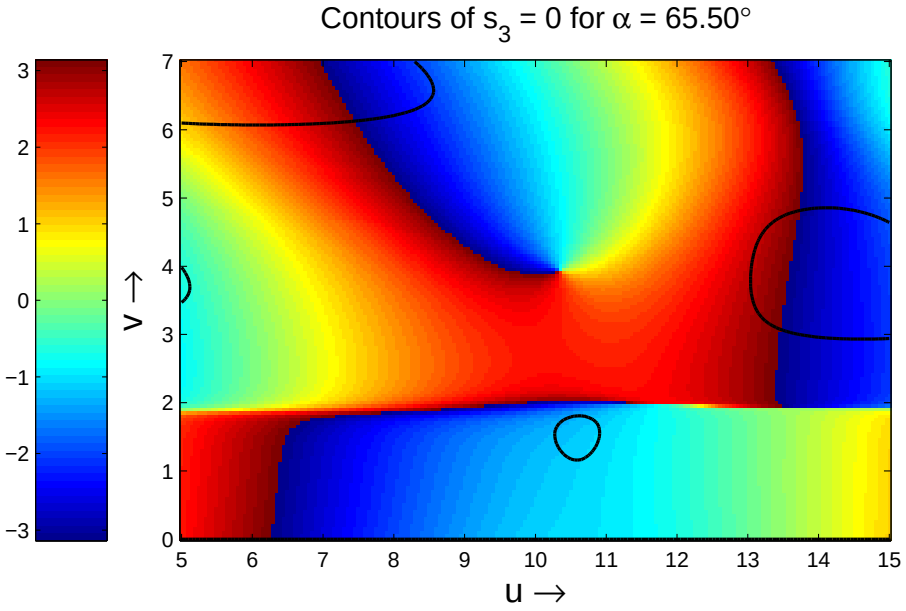

Figure B.61: A color-coded phase map of e_+ with L-lines (solid black curves) superposed and the semiaperture angle 65.50° with β kept fixed at 1.5.

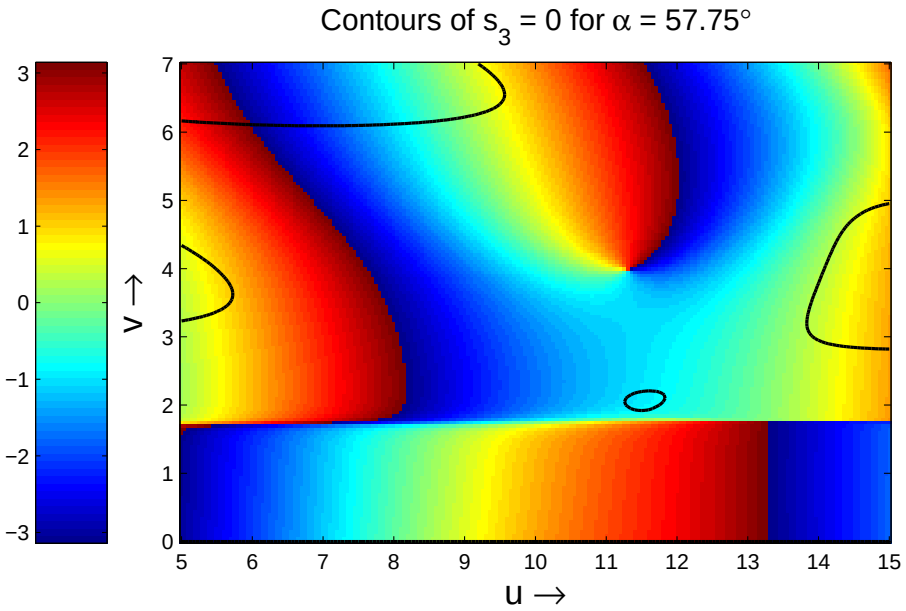

Figure B.62: A color-coded phase map of e_+ with L-lines (solid black curves) superposed and the semiaperture angle 57.75° with β kept fixed at 1.5.

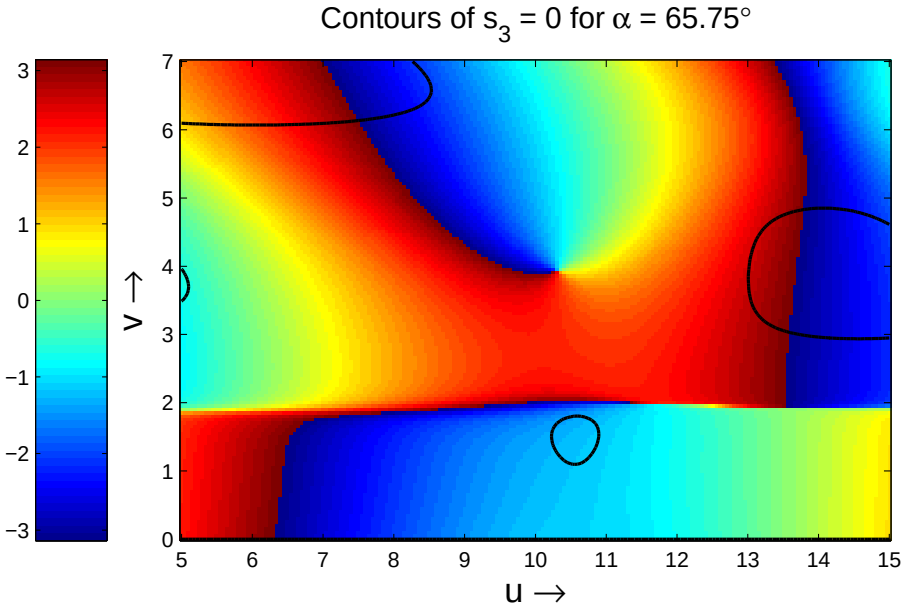

Figure B.63: A color-coded phase map of e_+ with L-lines (solid black curves) superposed and the semiaperture angle 65.75° with β kept fixed at 1.5.

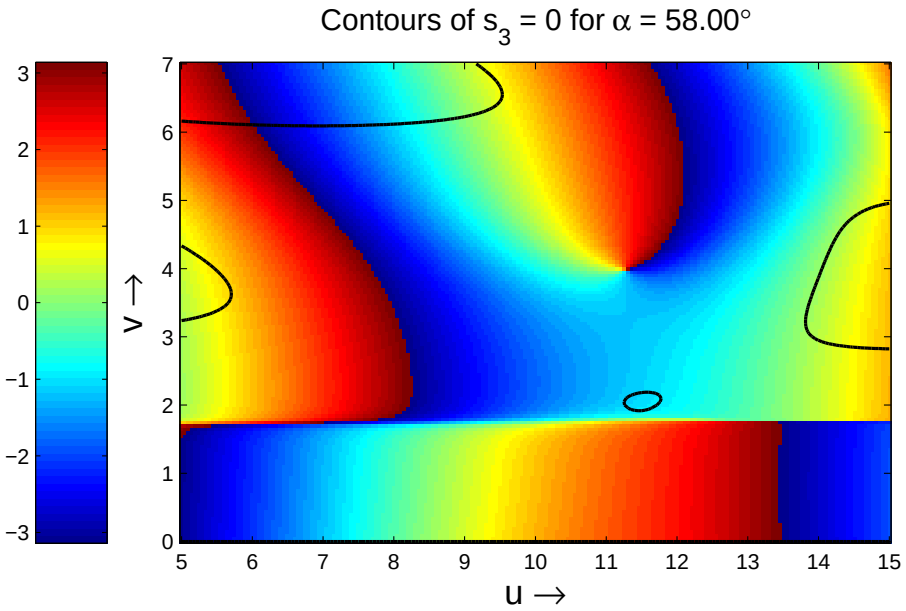

Figure B.64: A color-coded phase map of e_+ with L-lines (solid black curves) superposed and the semiaperture angle 58.00° with β kept fixed at 1.5.

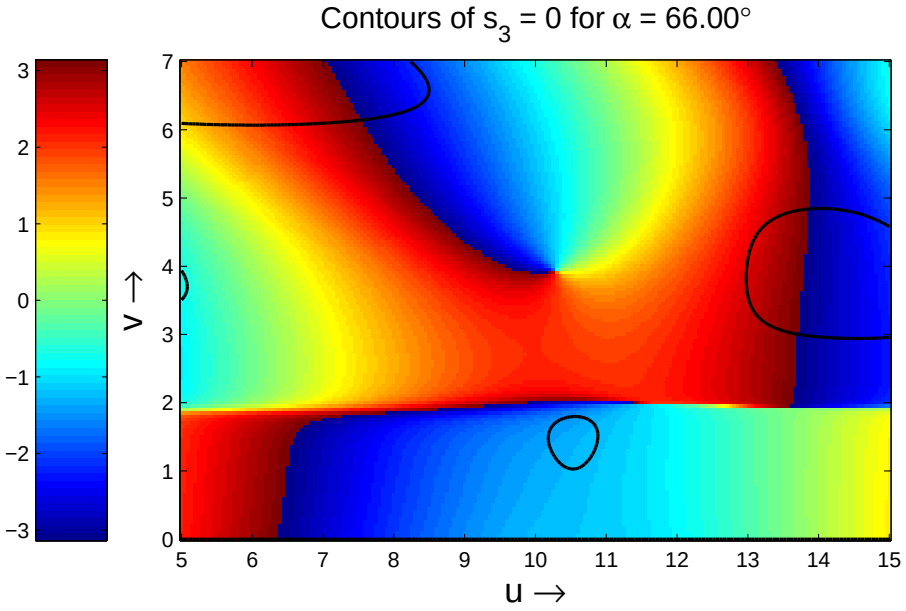

Figure B.65: A color-coded phase map of e_+ with L-lines (solid black curves) superposed and the semiaperture angle 66.00° with β kept fixed at 1.5.

REFERENCES

[1] J. Nye and M. Berry, "Dislocations in wave trains," Proc. R. Soc. Lond. A **336**, 165–190 (1974).

[2] J. Nye, *Natural Focusing and Fine Structure of Light* (IOP Publishing, Bristol, UK, 1999).

[3] M. Soskin and M. Vasnetsov, "Singular optics," Progress in Optics **42**, 219–276 (2001).

[4] G. Karman, M. Beijersbergen, A. van Duijl, and J. Woerdman, "Creation and annihilation of phase singularities in a focal field," Opt. Lett. **22**, 1503–1505 (1997).

[5] H. Schouten, T. Visser, D. Lenstra, and H. Blok, "Light transmission through a sub-wavelength slit: Waveguiding and optical vortices," Phys. Rev. E **67**(3), 36608 (2003).

[6] H. Schouten, T. Visser, G. Gbur, D. Lenstra, and H. Blok, "Creation and annihilation of phase singularities near a sub-wavelength slit," Opt. Expr. **11**(4), 371–380 (2003), `http://www.opticsexpress.org/abstract.cfm?URI=OPEX-11-4-371`.

[7] H. Schouten, T. Visser, G. Gbur, D. Lenstra, and H. Blok, "The diffraction of light by narrow slits in plates of different materials," J. Opt. A: Pure Appl. Opt. **6**, 277–280 (2004).

[8] D. Diehl and T. Visser, "Phase singularities of the longitudinal field components in high-aperture systems," J. Opt. Soc. Am. A **21**, 2103–2108 (2004).

[9] H. Schouten, G. Gbur, T. Visser, and E. Wolf, "Phase singularities of the coherence functions in Young's interference pattern," Opt. Lett. **28**, 968–970 (2003).

[10] G. Gbur and T. Visser, "Coherence vortices in partially coherent beams," Opt. Commun. **222**, 117–125 (2003).

[11] D. Fischer and T. Visser, "Spatial correlation properties of focused partially coherent light," J. Opt. Soc. Am. A **21**(11), 2097–2102 (2004).

[12] G. Gbur and T. Visser, "Phase singularities and coherence vortices in linear optical systems," Opt. Commun. **259**, 428–435 (2005).

[13] T. Visser and J. Foley, "On the wavefront spacing of focused, radially polarized beams," J. Opt. Soc. Am. A **22**(11), 2527–2531 (2005).

[14] D. Diehl, R. Schoonover, and T. Visser, "The structure of focused, radially polarized fields," Opt. Expr. **14**(7), 3030–3038 (2006), http://www.opticsinfobase.org/abstract.cfm?URI=oe-14-7-3030.

[15] R. Schoonover and T. Visser, "Polarization singularities of focused, radially polarized fields," Opt. Expr. **14**(12), 5733–5745 (2006), http://www.opticsinfobase.org/abstract.cfm?URI=oe-14-12-5733.

[16] M. Born and E. Wolf, *Principles of Optics: Electromagnetic Theory of Propagation, Interference and Diffraction of Light*, 7th ed. (Cambridge University Press, Cambridge, 1999).

[17] M. Berry and M. Dennis, "Polarization singularities in isotropic random vector waves," Proc. R. Soc. Lond. A **457**, 141–155 (2001).

[18] M. Dennis, "Polarization singularities in paraxial vector fields: Morphology and statistics," Opt. Commun. **213**, 201–221 (2002).

[19] I. Freund, A. Mokhun, M. Soskin, O. Angelsky, and I. Mokhun, "Stokes singularity relations," Opt. Lett. **27**(7), 545–547 (2002).

[20] M. Soskin, V. Denisenko, and I. Freund, "Optical polarization singularities and elliptic stationary points," Opt. Lett. **28**(16), 1475–1477 (2003).

[21] A. Mokhun, M. Soskin, and I. Freund, "Elliptic critical points: C-points, a-lines, and the sign rule," Opt. Lett. **27**(12), 995–997 (2002).

[22] K. Youngworth and T. Brown, "Focusing of high numerical aperture cylindrical-vector beams," Opt. Expr. **7**(2), 77–87 (2000).

[23] S. Quabis, R. Dorn, M. Eberler, O. Gloeckl, and G. Leuchs, "Focusing light to a tighter spot," Opt. Commun. **179**(1), 1–7 (2000).

[24] S. Quabis, R. Dorn, M. Eberler, O. Glöckl, and G. Leuchs, "The focus of light-theoretical calculation and experimental tomographic reconstruction," App. Phys. B **72**(1), 109–113 (2001).

[25] R. Dorn, S. Quabis, and G. Leuchs, "Sharper focus for a radially polarized light beam," Phys. Rev. Lett. **91**(23), 233,901 (2003).

[26] J. Foley and E. Wolf, "Wave-front spacing in the focal region of high-numerical-aperture systems," Opt. Lett. **30**(11), 1312–1314 (2005).

[27] B. Richards and E. Wolf, "Electromagnetic diffraction in optical systems. II. Structure of the image field in an aplanatic system," Proc. R. Soc. Lon. A **253**(1274), 358–379 (1959).

[28] J. Jackson, *Classical Electrodynamics*, 2nd ed. (John Wiley & Sons, New York, 1975).

[29] V. Denisenko, R. Egorov, and M. Soskin, "Measurement of the morphological forms of polarization singularities and their statistical weights in optical vector fields," J. Exp. Theor. Phys. Lett. **80**(1), 17–19 (2004).

[30] I. Freund, "Polarization singularity indices in Gaussian laser beams," Opt. Commun. **201**(4), 251–270 (2002).

[31] E. Copson, *An Introduction to the Theory of Functions of a Complex Variable* (Clarendon Press, London, UK, 1935).